

O VI EMISSION IMAGING OF A GALAXY WITH THE HUBBLE SPACE TELESCOPE: A WARM GAS HALO SURROUNDING THE INTENSE STARBURST SDSS J115630.63+500822.1

MATTHEW HAYES^{2,3}, JENS MELINDER³, GÖRAN ÖSTLIN³, CLAUDIA SCARLATA⁴, MATTHEW D. LEHNERT⁵, AND GUSTAV MANNERSTRÖM-JANSSON³

Accepted by the Astrophysical Journal

ABSTRACT

We report results from a new HST campaign that targets the O VI $\lambda\lambda 1032, 1038$ Å doublet in emission around intensely star-forming galaxies. The programme aims to characterize the energy balance in starburst galaxies and gas cooling in the difficult-to-map coronal temperature regime of $2 - 5 \times 10^5$ Kelvin. We present the first resolved image of gas emission in the O VI line. Our target, SDSS J115630.63+500822.1, is very compact in the continuum but displays O VI emission to radii of 23 kpc. The surface brightness profile is well fit by an exponential with a scale length of 7.5 kpc. This is ten times the size of the photoionized gas, and we estimate that about 1/6 the total O VI luminosity comes from resonantly scattered continuum radiation. Spectroscopy – which closely resembles a stacked sample of archival spectra – confirms the O VI emission, and determines the column density and outflow velocity from blueshifted absorption. The combination of measurements enables a large number of calculations with few assumptions. The O VI regions fill only $\sim 10^{-3}$ of the volume. By comparing the cooling time with the cloud sound-crossing time, the cooling distance with the size, and the pressure in the O VI and nebular gas, we conclude that the O VI-bearing gas cannot have been lifted to the scale height at this temperature, and must be cooling in situ through this coronal temperature regime. The coronal phase contains $\sim 1\%$ of the ionized mass, and its kinetic energy at a given instant is $\sim 1\%$ of the budget set by supernova feedback. However a much larger amount of the gas must have cooled through this phase during the star formation episode. The outflow exceeds the escape velocity and the gas may become unbound, but it will recombine before it escapes and become visible to Lyman (and O I) spectroscopy. The mapping of this gas represents a crucial step in further constraining galaxy formation scenarios and guiding the development of future astronomical satellites.

Subject headings: galaxies: evolution — galaxies: starburst — galaxies: halos — galaxies: ISM — Galaxies: individual: J1156+5008

1. INTRODUCTION

Gaseous outflows from galaxies, taking the form of large-scale ‘superwinds’, become commonplace once a certain threshold surface density of star-formation is exceeded ($\Sigma_{\text{SFR}} \gtrsim 0.1 \text{ M}_{\odot} \text{ yr}^{-1} \text{ kpc}^{-2}$; Heckman 2002). For local galaxies considered starbursts, outflows of high- and low-ionization gas are effectively ubiquitous (Heckman et al. 1990; Rupke et al. 2005; Martin 2005; Heckman et al. 2011; Rivera-Thorsen et al. 2015), and comparable results are also found at higher redshifts (e.g. Weiner et al. 2009; Rubin et al. 2010; Erb et al. 2012; Rubin et al. 2014), including a similar threshold surface density of star-formation (Kornei et al. 2012).

The most likely mechanism for driving large-scale out-

flows begins with the ejection of fast-moving material in the winds of the most massive stars, and the ejecta of core-collapse supernovae. In dense star forming regions these ejecta collide, the gas shock heats and thermalizes, and produces a hot plasma in the nuclear regions. With temperatures of around 5×10^7 K – seen observationally using iron lines in the hard X-ray bands (e.g. Strickland & Heckman 2009) – this gas rapidly expands and flows outwards from the (central, likely nuclear) star-forming regions, imparting energy and momentum onto surrounding media, and sweeping up material in various phases (Chevalier & Clegg 1985; Murray et al. 2005). Due to the hydrodynamical interactions between hot and cold gas phases, and compression, heating and enhanced cooling at the interfaces, such outflows are genuine multiphase phenomena (McKee & Ostriker 1977; Hopkins et al. 2012; Braun & Schmidt 2012; Thompson et al. 2016). Indeed outflow signatures are observed in almost all phases from starbursts and active galactic nuclei (Grimes et al. 2009; Rivera-Thorsen et al. 2015; Feruglio et al. 2015; Chisholm et al. 2015; Beirão et al. 2015).

This feedback from star formation is probably a vital ingredient in the shaping of a number of galaxy scaling relations. Feedback is believed to be the main source for regulating the subsequent star formation in galaxies, preventing too many stars from being formed too early. In balancing the rate at which gas is accreted onto

¹ Based on observations made with the NASA/ESA Hubble Space Telescope, obtained at the Space Telescope Science Institute, which is operated by the Association of Universities for Research in Astronomy, Inc., under NASA contract NAS 5-26555. These observations are associated with program #13656.

² matthew@astro.su.se

³ Stockholm University, Department of Astronomy and Oskar Klein Centre for Cosmoparticle Physics, AlbaNova University Centre, SE-10691, Stockholm, Sweden.

⁴ Minnesota Institute for Astrophysics, School of Physics and Astronomy, University of Minnesota, 316 Church Str. SE, Minneapolis, MN 55455, USA.

⁵ Institut d’Astrophysique de Paris, UMR 7095, CNRS, Université Pierre et Marie Curie, 98bis boulevard Arago, 75014, Paris, France.

halos, it is responsible for keeping galaxies on the approximately linear relationship between star formation rate (SFR) and stellar mass (M_*): the ‘main sequence’. Consequently, stellar feedback and its efficiency are likely responsible for shaping at least the low luminosity end of the galaxy luminosity function (e.g. Efstathiou 2000; Benson et al. 2003). Moreover, since outflows are driven in part by supernova ejecta, they are likely to be metal-enriched compared to the interstellar medium (ISM). If winds escape from galaxies then feedback will also impact the shaping of the relationship between galaxy metallicity and mass (e.g. Tremonti et al. 2004; Andrews & Martini 2013).

Since galaxy formation simulations are generally regarded as successful if they can reproduce the above scaling relations (see Somerville & Davé 2015, for a review), it must be vital that the prescriptions of feedback are as precise as possible. Not only must one know whether winds will escape from the halos of the galaxies that launch them (thereby enriching the intergalactic medium, IGM, with metals), but also what phase the gas will be in if and when it does. I.e. if it will remain in a hot low-density phase, in which case it cannot contribute to subsequent star-formation anywhere, or if it will cool, recombine, and perhaps re-accrete, and rejoin the reservoir of available material. From the observational perspective this requires us to determine the spatial distribution and kinematics of gas in the ISM and circumgalactic medium (CGM). Since the outflows are likely multi-phase, existing over a wide range of temperatures that account for different amounts of the energy and mass, ideally one would do this with as many tracers as possible, from the hottest gas that drives that initial stages of the outflow, to the cold gas phases that are entrained.

The hottest gas – from roughly a million K and upwards – may be traced by X-ray emission, while from temperatures of a few times 10^4 K observers utilize nebular line emission in the optical, transitions of low ionization stage metals in the far ultraviolet, and molecular lines in the radio (in order of decreasing temperature). This leaves a gap of between a few 10^4 and 10^6 K, that can only be probed using the resonant transitions of highly ionized metals in the far ultraviolet. At these temperatures, of several 10^5 K the strongest and most readily available is the doublet of O VI at $\lambda\lambda = 1032, 1038$ Å in the restframe. Such species remain vital, being the main coolants of metal enriched gas at these temperatures (e.g. Sutherland & Dopita 1993), and thus its availability and distribution governs the nature and evolution of gas in galaxy halos. In this paper we address this phase directly, by measuring the morphology of $T \approx 300,000$ K gas in the halo of a strongly star-forming galaxy with the Hubble Space Telescope (HST).

It is hard to understate the relevance of O VI in this context. Oxygen is the third most abundant element in the Universe, is produced by stars, and thus should accurately trace the growth of metals created through stellar nucleosynthesis, the majority of which is ejected into the ISM. However, when observers attempt to account for the metals in galaxies, a significant deficit is usually found; this holds for a variety of galaxy selection functions and over a wide range of redshifts (Prochaska et al. 2003; Bouché et al. 2005; Zahid et al. 2012). Focusing

specifically on the metals traced by O VI, recent studies with the *Cosmic Origins Spectrograph* (COS) on HST have proven pivotal in unveiling the reservoir of warm oxygen, as the metals are expelled to large galactocentric radii. Specifically the *COS-Halos* survey (Tumlinson et al. 2011, 2013) has precisely quantified the amount of O VI gas in galaxy halos: summing the oxygen found in stars, dust, and various gas phases, Peeples et al. (2014) find that only ≈ 30 % on average of the metals produced by stars can be accounted for. Particularly in lower mass galaxies, $M_* \approx 10^{9.5} M_\odot$, the bulk of this oxygen resides in a diffuse phase, in circumgalactic environments at distances of up to ~ 150 kpc (see also Prochaska et al. 2011). Only for these lower mass galaxies, and under the most optimistic of assumptions, can the metal budget be recovered.

The identification of warm metals has been a major avenue of exploration with mid and high resolution ultraviolet spectrographs, such as the *Far Ultraviolet Spectroscopic Explorer* (FUSE) and the *Space Telescope Imaging Spectrograph* (STIS) and COS on HST (Tripp et al. 2000; Hoopes et al. 2002; Sembach et al. 2004; Tumlinson et al. 2005; Prochaska et al. 2006; Danforth et al. 2006; Tripp et al. 2008; Thom & Chen 2008; Wakker & Savage 2009; Savage et al. 2011; Tumlinson et al. 2013; Stocke et al. 2013; Savage et al. 2014). By targeting metal enriched gas at $T \sim 10^{5.5}$ K, these studies are intimately linked with the more general problem of absent baryonic matter at low- z – the ‘missing baryons problem’ (see Bregman 2007, for a review). While enormously successful, absorption line studies rely upon the presence a UV-bright background quasar along the line-of-sight, and two limitations are implicit in the method. Firstly appropriately bright QSOs are rare, and not any object can be observed; while disks that form stars may be abundant at low- z , extreme starbursts are not, which means appropriate QSO-starburst projections will be particularly rare. Such starbursts may be enormously important because these are the objects that drive the strongest winds at low- z (Heckman et al. 2011, 2015). Moreover, they share many of their properties with galaxies at $z > 1$ where the bulk of the cosmic metals were produced, and indeed metal enrichment in the universe must have begun early (e.g. Cen & Ostriker 2006). The second drawback is that unless the galaxy is very extended on the sky, the average galaxy will not have a sufficiently bright background QSO and, if it does, a measurement will be possible (probabilistically) on only one sightline. Thus galaxies can only be studied population-wise, by combining single sightlines through many objects.

Both of the above issues could be overcome if we could map the O VI gas in emission, and infer column and volume densities from the surface brightness. Indeed detecting the warm-hot intergalactic medium via O VI emission is one of the goals of the *Faint Intergalactic Redshifted Emission Balloon* (FIREBALL, Tuttle et al. 2010) and *Advanced Technology Large Aperture Space Telescope* (ATLAST, Postman et al. 2010), albeit with more explicit focus on extended intergalactic gas and the large-scale structure of the cosmic web. With current facilities the detection remains a particularly challenging task, because the densities in the coronal O VI phase are low, and the n_e^2 dependence of the emissivity sug-

gests that the surface brightness would also be low. The O VI $\lambda\lambda 1032, 1038$ Å doublet has, however, been detected in emission in a small number of cases: NGC 4631 (Otte et al. 2003) and Haro 11 (Grimes et al. 2007) both exhibit irrefutable O VI emission lines which lends some confidence to the prospect of mapping the gas.

A second challenge is that to map the emission line, a far ultraviolet narrowband filter or integral field spectrograph would be needed, and no such dedicated hardware is currently available. However over the last decade our group has developed methods of synthesizing narrowband filters using existing channels of the *Solar Blind Channel* (SBC) of the *Advanced Camera for Surveys* (ACS) on HST, which we have verified many times by targeting the Ly α line of H I (Hayes et al. 2005, 2009, 2013).

In this paper we present the first O VI emission-line imaging observations of a star-forming galaxy: SDSS J115630.63+500822.1. The combination of HST emission imaging and absorption spectroscopy allows us to calculate a large number of properties relevant for the warm coronal gas phase, how it is excited, and what its future will be. As we present only one single galaxy, this stage of the project can be regarded as a pilot study, although it will be expanded in the current observing cycle of HST. We have selected an intense local starburst that hitherto has not been studied in much detail, although it does enter the sample of highly excited blue compact galaxies studied by Chung et al. (2013). We present the motivation for selecting this target in Section 2 and derive a number of common physical properties from the optical spectrum and spectral energy distribution. The method used to isolate the O VI line is presented in Section 3, together with a description of the HST observations. Section 4 presents the data reduction and processing. In Section 5 we present the results, that show a large extended halo of excess emission in the on-line bandpass and a faint emission line in the spectrum that we interpret as O VI $\lambda 1038$ Å. In Section 6 we present an analysis of archival COS spectra of starbursts at similar redshifts; we perform a stacking analysis to show that the same spectral emission feature is also visible in other galaxies. Section 7 presents a set of calculations in which we estimate many properties of warm gas. These include the size of the emitting regions, the mass in this phase, the cooling time and the ultimate fate of the gas. These are the main results of the Paper. In Section 8 we compare the observational results obtained here with the other two detections of O VI emission from galaxies. Finally in Section 9 we present a summary and our conclusions. We adopt cosmological parameters of $H_0 = 70$ km s $^{-1}$ Mpc $^{-1}$, $\Omega_M = 0.3$, and $\Omega_\Lambda = 0.7$. Any magnitudes will be given in the AB system (Oke & Gunn 1983).

2. THE TARGET GALAXY: J1156+5008

The target galaxy has never been discussed in detail before, so we here present the method and motivations we used to select it, and some of its basic (‘standard’) measured and derived properties.

2.1. Motivations and Selection

Only two individual star-forming galaxies are known to emit O VI: NGC 4631 (Otte et al. 2003) and Haro 11

(Bergvall et al. 2006; Grimes et al. 2007). Prior to our study we had no information that we could use to select targets. Moreover, both of these previous detections were in spectroscopic observations, made with the FUSE. However the FUSE had a large (30×30 arcsec) square aperture and provided no spatial information that could guide us – the only ‘morphological’ information available was that O VI emission is observed away from the disk in NGC 4631. Without knowledge of what galaxies we should target or where best to observe them, we selected the star-forming galaxy most likely to emit O VI based mainly upon results from the FUSE archive and the *COS-Halos* survey (Tumlinson et al. 2013).

Tumlinson et al. (2011) demonstrated that O VI absorption was ubiquitous in the halos of star-forming galaxies but not necessarily present in passive systems. Within their star-forming sample, they identified a trend in which the O VI column density (N_{OVI}) increases with increasing sSFR. While this does not tell us that the volume density (the important quantity for emissivity) also increases, we argued that a correlation would most likely be positive. However when studying O VI absorption against the UV continuum of galaxies themselves, the ubiquity of N_{OVI} features does not extend to the low-mass dwarf starbursts: 1Zw 18 and SBS 0335–052 do not show O VI absorption in FUSE spectra (Grimes et al. 2009). We suspect the reasons for this are firstly that these galaxies are extremely metal poor ($\sim 1/40$ the solar value in most metallic ions), and secondly that the starbursts are particularly young and they have not yet developed large-scale supernova-driven outflows to collisionally excite the warm phase. Since the winds and chemical enrichment are primarily the result of supernova explosions, the youth of the star-formation episodes may make them poor candidates in which to make O VI detections. In contrast, however, the luminous blue compact galaxy Haro 11 still emits O VI (Grimes et al. 2007), despite being under-abundant in nebular metals for its luminosity (Östlin et al. 2015). Thus a lower metallicity galaxy may not be a bad candidate per se, provided the current SFR is high and star formation has been ongoing for some Myr.

Arguing that both SFR and sSFR should be maximized, we searched the *Sloan Digital Sky Survey* (SDSS) spectroscopic Data Release 12 (Ahn et al. 2014) for galaxies that have:

1. H α equivalent width ($W_{\text{H}\alpha}$) above 50 Å. This guarantees current active star formation.
2. Redshift in the range 0.23 to 0.29. This shifts the O VI doublet into the wavelength region where it can be efficiently observed with HST (this is described in detail in Section 3.1).
3. Less than 0.1 magnitudes of Milky Way extinction in the u -band. This minimizes foreground extinction that would absorb at far UV wavelengths, and maximizes the efficiency of the observations.

We cross-correlated this first selection with UV photometric catalogues from Data Release 6 of the *Galaxy Evolution Explorer* (GALEX) archives. We computed FUV luminosities using the SDSS redshifts, and converted the result into star-formation rates (SFR, Kennicutt 1998).

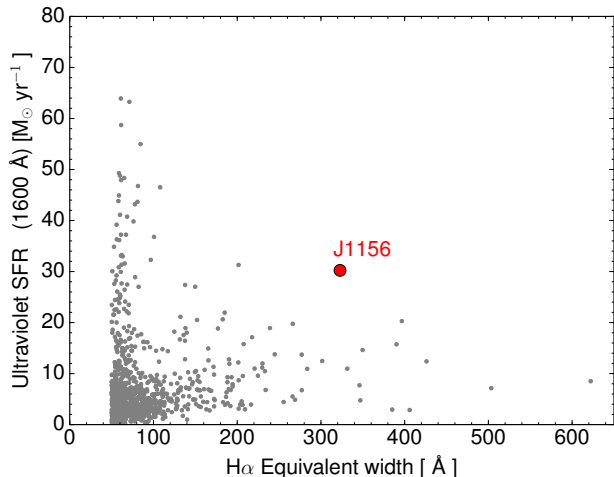


Figure 1. The UV SFR vs $H\alpha$ EW of our SDSS+GALEX catalogues. The red spot shows J1156.

This gave the selection diagram shown in Figure 1. In this diagram it is clear that few galaxies have both high SFR and $W_{H\alpha}$, and the upper right portion of the diagram is under-populated: for example, only two objects have both $W_{H\alpha}$ above 200 Å and SFR exceeding $30 M_{\odot} \text{ yr}^{-1}$. We selected SDSS J115630.63+500822.1, which is shown in red in Figure 1.

2.2. Basic Properties of J1156

SDSS J115630.63+500822.1 (hereafter J1156) lies at a distance of 1200 Mpc ($z = 0.235$) and was selected to maximize the chances of detecting O VI emission. It has a star formation rate ~ 40 times higher than the Milky Way ($40 M_{\odot} \text{ yr}^{-1}$), and an optical spectrum that is rich with strong emission lines suggestive of active star formation.

The SDSS image and spectrum of J1156 are shown in Figure 2. We extract the UV and optical magnitudes from GALEX and SDSS and subtract the contributions of the strong optical emission lines of [O II] $\lambda 3727$ Å, $H\beta$, [O III] $\lambda\lambda 4959, 5007$ Å and $H\alpha$ based upon the equivalent widths measured the SDSS. We then proceed to fit the spectral energy distribution (SED) with with Hyper-z (Bolzonella et al. 2000) using Bruzual & Charlot (2003) templates with metallicity $Z = 0.004$ (closest to the nebular metallicity) and a Salpeter initial mass function (IMF). Derived properties are listed in Table 1.

The FUV absolute magnitude, M_{FUV} , is -21.2 (AB system), which is close to the characteristic luminosity, L^* , of Lyman Break Galaxies at $z = 3$ (Reddy & Steidel 2009). The UV-to-optical integrated SED is flat in the AB magnitude system (SDSS z -band magnitude is within 0.2 mags of the GALEX FUV magnitude), indicating a very blue, young stellar population with little extinction. The galaxy has a UV SFR of $\approx 30 M_{\odot} \text{ yr}^{-1}$ ($H\alpha$ SFR $\approx 25 M_{\odot} \text{ yr}^{-1}$, and neither value is corrected for extinction) and a stellar mass of $\sim 1.5 \times 10^9 M_{\odot}$, giving a specific SFR (sSFR) of $2 \times 10^{-8} \text{ yr}^{-1}$. Alternatively, J1156 would have built its current stellar mass in just 50 Myr at the current SFR.

From the SDSS spectrum we measure the fluxes of a number of commonly used nebular emission lines. We compute the $H\alpha/H\beta$ ratio to be 3.3, which is

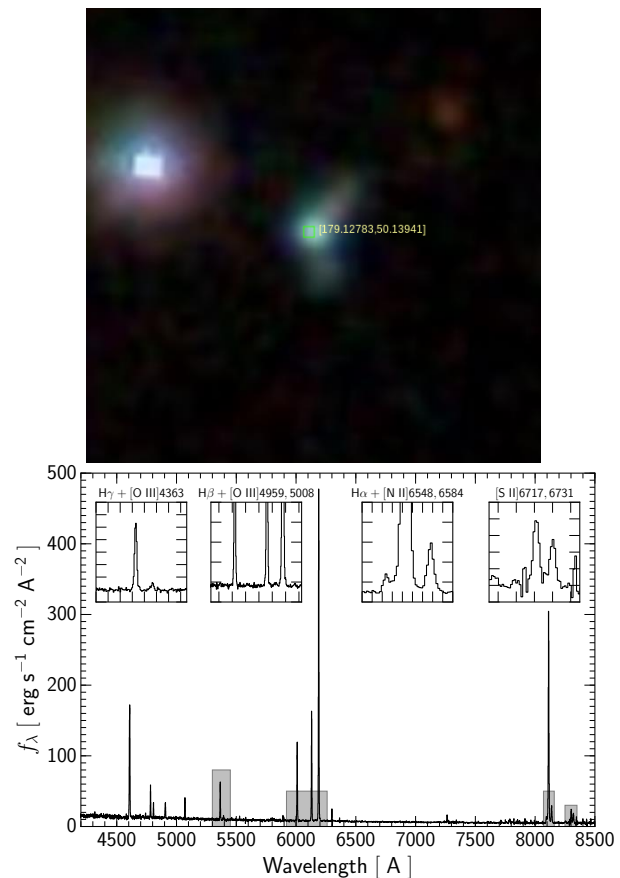


Figure 2. SDSS Data for J1156. *Upper* shows the color composite image, and *lower* the optical spectrum in the observer frame. The galaxy is very compact at optical wavelengths, and the spectrum is characterized by a blue continuum with very strong, narrow optical emission lines. Zoomed regions are illustrated by gray shaded boxes, and show some of the emission lines we use in this paper.

somewhat higher than the value of 2.9 expected for unreddened gas at 10^4 K (Osterbrock 1989), and indicates there is little internal extinction of the nebular gas. We further compute the oxygen abundance using both the electron temperature (T_e) sensitive method from the auroral [O III] $\lambda 4363$ Å line and strong-line calibrations, and compute the electron density (n_e) from the relative strengths of the components of the [S II] $\lambda\lambda 6717, 6731$ Å doublet using the TEMDEN task in the STSDAS.ANALYSIS.NEBULAR package of Pyraf. The [O II] $\lambda\lambda 3726, 3729$ Å doublet, which also traces n_e , unfortunately cannot be deblended at the resolution of the SDSS spectrum. From the product of T_e and n_e we measure the pressure, P . All of these properties are listed in Table 1.

3. OBSERVATIONS WITH THE HUBBLE SPACE TELESCOPE

3.1. Isolating ultraviolet emission lines in imaging mode

Isolating line emission requires a narrowband filter, but no conventional narrowbands exist on the ACS/SBC. Instead we synthesize them using adjacent pairs of long-pass filters, as shown in Figure 3. The long-pass filters are all described by a sharp, almost step-like, cut-on at the blue side, and each has an extended red wing that results from the declining quantum efficiency of the solar blind MAMA detector. The subtraction of adja-

Table 1
Derived Properties of J1156

Property (1)	Derived (2)	16 th %-ile ^a (3)	84 th %-ile ^a (4)	Unit (5)
SFR (UV) ^b	18.2	18.0	18.5	M _⊙ yr ⁻¹
SFR (Hα) ^b	26.2	25.5	27.0	M _⊙ yr ⁻¹
SFR (Hα corr.) ^{b,d}	39.0	33.1	44.8	M _⊙ yr ⁻¹
SFR (SED) ^c	35.3	35.2	65.4	M _⊙ yr ⁻¹
Stellar mass (SED) ^c	1.5	1.4	2.5	10 ⁹ M _⊙
SFH (SED) ^c		5 Myr Exponential SFR decline in 65% of cases		
Stellar age (SED) ^c	11.5	10.0	39.0	Myr
E_{B-V} (SED fit) ^{c,d}	0.14	0.13	0.15	Magnitudes
E_{B-V} (Hα/Hβ) ^d	0.13	0.08	0.18	Magnitudes
Metallicity (O3N2) ^e	8.34	8.05	8.62	12+log(O/H)
Metallicity (T_e) ^e	7.87	7.70	8.05	12+log(O/H)
T_e ([O II]) ^e	1.34	1.19	1.50	10 ⁴ K
T_e ([O III]) ^e	1.48	1.27	1.72	10 ⁴ K
Electron density [S II] ^f	4.65	...	44.2	cm ⁻³
Pressure (p/k_B)	6.88	...	65.4	10 ⁴ K cm ⁻³

Note. — Col. 2 represents the derived value, while Cols 3. and 4. present the limits of the 16th and 84th percentiles. References and clarifications:

^a Errors on quantities derived direct from photometry or line ratios are estimated by standard error propagation; errors on T_e and SED-fit quantities are derived by Monte Carlo simulations.

^b SFR (Kennicutt 1998) assuming a Salpeter (1955) stellar initial mass function (IMF) with lower (higher) mass cutoff of 0.1 (100) M_⊙, and solar metallicity.

^c Properties derived from spectral energy distribution fitting are calculated using global photometry derived within six Petrosian radii, calculated in the far UV. We used the Hyper-z SED fitting code (Bolzonella et al. 2000) using Bruzual & Charlot (2003) templates with metallicity Z=0.004 and the same IMF as above.

^d Dust corrections use the Calzetti et al. (2000) prescription.

^e Metallicities are derived using the Yin et al. (2007) calibration of the O3N2 method, and the algorithm presented in the same paper for the T_e method.

^f Electron density is calculated from the ratio of $\lambda = 6717/6731$ Å components of the [S II] doublet, using the TEMDEN task in the STSDAS.ANALYSIS.NEBULAR package of Pyraf. The observed ratio is slightly higher than the low-density plateau (Osterbrock 1989), so we adopt the lowest density quoted.

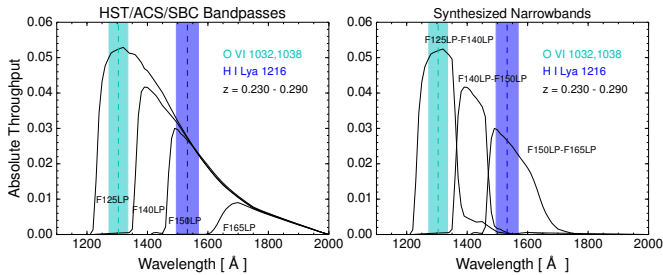


Figure 3. The isolation of UV emission lines with ACS/SBC. *Left*: total throughput of the ACS/SBC filters: F125LP, F140LP, F150LP, and F165LP. The LP filters all share the same red wing but have different blue cut-on wavelengths, so subtraction of adjacent pairs reveals the well-defined narrow bandpasses (*right*) that we use to isolate O VI. At $z = 0.23 - 0.29$, F140LP subtracts the continuum from O VI, which falls only in F125LP.

cent filter pairs therefore produces well-defined “pseudo-narrowband” filters (Hayes et al. 2009), as illustrated in Figure 3. The left panel shows the bandpass profiles, and the right panel shows the profiles that result from pair-subtraction. A further advantage of the pair-subtraction is that, because each bandpass shares the same red wing, each also has the same red-leak that is then subtracted. Therefore, no residual signal can be attributed to red-leaks, as it would be present in all the images taken with long-pass filters.

We have used this method for continuum-subtracting H I Lyα ($\lambda_{\text{rest}} = 1215.67$ Å) images in the *Lyman Alpha Reference Sample* (LARS, Hayes et al. 2014; Östlin et al. 2014) in total we have applied it to around 50 starburst galaxies selected to redshift Lyα into the narrowband

windows. In designing the O VI study we used the same strategy, but instead applied a redshift constraint to shift the O VI doublet into the F125LP–F140LP window. This sets the redshift range of $z = 0.23 - 0.29$, as mentioned in Section 2, and conveniently also redshifts the H I Lyα line into the wavelength region isolated by the F150LP–F165LP pair (Figure 3), which we also obtained.

3.2. HST Observations and Strategy

3.2.1. Imaging Data

J1156 was observed in both imaging and spectroscopic modes. Data can be found in the *Mikulski Archive for Space Telescopes* (MAST), under GO 13656. Table 2 summarizes the observations, which were performed with:

- The *Advanced Camera for Surveys* (ACS), using long-pass filters of the Solar Blind Channel (SBC) in the ultraviolet, and tunable linear ramp filters of the Wide Field Channel (WFC) in the optical.
- The *Wide Field Camera 3* (WFC3), using UVIS broadband filters in the optical.
- The *Cosmic Origins Spectrograph* (COS), using the FUV channel and the G130M grating to obtain medium resolution spectroscopy.

Observations of O VI and its adjacent continuum must be particularly deep: for this program we have dedicated 16 spacecraft orbits to (combined) imaging in F125LP and F140LP, which were divided into eight visits of two

Table 2
HST Observing Log.

Instrument (1)	Filter/Grating (2)	Central Wavelength (Å) (3)	Exposure Time (s) (4)	Purpose / Comment (5)
ACS/SBC	F125LP	1438	15,864	O VI online / 6 of 8 visits
ACS/SBC	F140LP	1528	17,304	O VI continuum / 6 of 8 visits
ACS/SBC	F150LP	1612	2,742	Ly α online
ACS/SBC	F165LP	1763	5,442	Ly α continuum
WFC3/UVIS	F390W	3923	912	Restframe U -band
WFC3/UVIS	F475W	4773	700	Restframe B -band
ACS/WFC	FR601N	6010	1,419	H β narrowband
ACS/WFC	FR782N	8111	700	H α narrowband
WFC3/UVIS	F850LP	9167	700	Restframe I -band
COS/FUV	G130M	1318	2,360	1150-1450 Å spectroscopy

Note. — Imaging filters are ordered by increasing central wavelength; the COS spectrum is the last entry. For the F125LP and F140LP frames, only data from six of the eight visits was used because of noticeable dark current in the other two.

orbits each. We worked closely with the contact scientists and scheduling team at the Space Telescope Science Institute (STScI) to ensure that these visits were executed only when the SBC had not been used during the previous 24-hour period. This was to guarantee that the readout amplifiers had been switched off for a significant time⁶, which allows them to cool. This reduces the dark current, which is strongly temperature-dependent, to a level that is below the background. However this visit execution requirement was not fulfilled for two of the F125LP+F140LP visits (02 and 05), resulting in significantly increased background. We excluded data that were obtained during these two visits.

For F125LP+F140LP we executed a 16-point dithering pattern, with two positions performed in each of the eight visits. The 16 points dither over a 4×4 -pointing grid, stepped at each position by 3 arcsec in detector coordinates. No orientation constraint was placed on the roll angle of the telescope, and hence not only are the dithers large, but the roll angle also varies. This strategy was designed to minimize residuals from the flatfielding by averaging over 16 well-separated detector positions. In reality, only 12 pointings were used for the final stacked images because two visits were removed. In each orbit we executed the F125LP observation during orbital night (‘shadow’) to minimize the background due to the geocoronal oxygen emission lines near 1304 Å.

SBC imaging of Ly α and the adjacent continuum (see Figure 3) were executed in one orbit for F150LP and two orbits in the less sensitive F165LP. WFC3/UVIS imaging in F390W, F475W, and F850LP was accomplished in a single orbit, using two exposures for each filter and a half-pixel dithering strategy in x and y detector coordinates. ACS/WFC ramp filter imaging to obtain H α and H β narrowband frames were also accomplished in one orbit with half-pixel dithering. For WFC3 and ACS CCD imaging we post-flashed each exposure with the number of electrons needed to reach the recommended background levels that minimized the charge transfer inefficiency at read-out.

3.2.2. Spectroscopic Data

Spectroscopic data with the COS were taken with the G130M grating, which provides medium resolution spec-

troscopy between 1150 and 1450 Å. The effective area of G130M reaches a maximum near 1250 Å, precisely the wavelength region to which our narrowband imaging using F125LP–F140LP is tuned. The grating provides a spectral resolving power (assuming a point source) of $R \approx 20,000$ at 1250 Å, or around 15 km s^{-1} . This enables us to resolve interstellar emission and absorption profiles on the galaxy scale, and indeed all lines are clearly resolved in the spectra. COS observations were accomplished in a single orbit using the 1309 Å central wavelength setting. All four FP-POS settings were used to dither each spectral image in the dispersion direction and average over fixed-pattern noise, gain sag, and remove grid wire shadows. The target acquisition worked flawlessly, placing the brightest UV point in the center of the Primary Science Aperture to within 0.05 arcsec.

4. DATA REDUCTION AND PROCESSING

4.1. Imaging Data

4.1.1. Initial Reduction of the Science and Weight Frames

We began our data reduction process by obtaining all images from the MAST, taking data that had been pipeline-processed to the point of flat-field correction (i.e. the `raw.fits` and `flt.fits` frames).

CCD channels (WFC3/UVIS and ACS/WFC) have imperfect charge transfer efficiency, producing streak-shaped artefacts around bright objects (and mostly cosmic ray hits), particularly if the dominant source of noise is from readout. While we did post-flash our observations to minimize this, many of these streaks remain in the individual `flt` images. For the ACS/WFC images, a postiori CTE correction is performed by the pipeline, but for the WFC3/UVIS frames this is not the case. For UVIS images we process the `flt` images with the `wfc3uv.ctereverse_parallel` code, developed at STScI.

The next step is to register all the frames onto a common pixel grid and co-add frames from each filter. For this we make use of the `drizzlepac` software, where we used `astrodrizzle` to correct for distortions and register all frames onto a grid of 0.1 arcsec pixels. Small shifts in the world coordinate system, that arise from the use of different guide stars in different visits, were rectified with the `tweakreg` package, and images were re-drizzled from scratch to minimize the number of times the pix-

⁶ ACS Instrument Science Report ACS 2009-02

els were resampled. All frames were then matched to the F390W filter, as it is the most central filter in (logarithmic) wavelength space. The inverse variance weight map for each filter was saved in addition to the combined science image.

We performed an additional sky subtraction in the reduced science frames. We computed the sky values in boxes of several square arcsec, which were positioned around the galaxy (~ 10 arcsec away), and avoided obvious features. We then approximated the sky by a flat surface that could vary in tilt, described by a first order polynomial in x and y with no cross-term. This surface was subtracted from the science frames, providing residual sky that was an order of magnitude below the sky noise in the same boxes where the sky was measured.

4.1.2. Matching the Point Spread Functions

We estimate the line-only flux in the O VI lines using several methods, that we describe in Section 4.1.4. Some of these methods require the use of longer-wavelength data, obtained from the WFC3/UVIS and ACS/WFC cameras, and hence rely on precise matching of the point spread functions (PSF) of the images. This is particularly important because the PSF of the SBC moves significant power to radii larger than ~ 0.5 arcsec, and produces extended wings that are not present in data from the optical cameras.

We first construct PSF models for all of the filters used in the study. For the optical filters we use TinyTim models which are placed into the (un-drizzled) pipeline-processed `flt` frames. We then drizzle the frames in the same way as the actual data frames and extract PSF models from the drizzled output. This procedure does not work for the FUV data obtained with SBC because the TinyTim models are not accurate enough (especially not in the extended wings). For the SBC data we instead build PSF models from stacks of stars observed in a stellar cluster (see Appendix A for details). We then proceed to make a maximum width PSF model by normalizing all models to the same peak flux and stack them by maximum pixel value.

We then find convolution kernels that match the PSFs for all of the filters to the maximum width model. Each kernel is built up from a set of delta functions and we find the optimum matching kernel by least squares optimization. The method is similar to the technique described in Becker et al. (2012) and details will be presented in a forthcoming paper (Melinder et al. in preparation). The method is very sensitive to noise in the input PSFs and using models is therefore required to compute the matching kernel. The drizzled and registered images are then convolved with the optimal matching kernels which result in a set of images matched to a common PSF.

4.1.3. Voronoi Tessellation

As is often the case for imaging of extended sources, the signal-to-noise ratio (SNR) is high in the central regions but low in the outskirts. In this study we are particularly concerned about the lower surface brightness, diffuse regions. We therefore use adaptive binning tools to aggregate pixels together as a function of local SNR, until a threshold SNR is met. Hence in the central regions of the galaxy bins are small, and the exquisite spatial resolution of HST is preserved, while in the outskirts we

sacrifice some of the spatial resolution in favor of higher SNR. The advantage of binning, as opposed to smoothing, is that every pixel contributes once and only once to a bin, and thus mathematical treatment of the noise is straightforward.

We made use of the **Weighted Voronoi Tessellation** binning algorithm by Diehl & Statler (2006), which is a generalization of the Cappellari & Copin (2003) Voronoi binning algorithm. We adopted the F125LP image as a reference image because it contains both UV continuum and O VI, and binned together pixels until either a minimum SNR of 10 was obtained, or bins reached a maximum size of 100 pixels (1 square arcsecond). With the binning pattern computed for the F125LP frame, we applied the same pattern to images taken in all the other filters, again storing the science image and the inverse variance weight map. All photometric quantities reported in this article are derived from the tessellated frames.

4.1.4. Subtracting the Continuum from O VI

The technique described in Section 3.1 isolates a narrow bandpasses in the UV, but we remain concerned about several issues that enter the estimation of the continuum in F125LP filter. In previous studies where we have targeted Ly α , we have explored and discussed different methods of continuum-subtracting SBC imaging data, using various assumptions and models (Hayes et al. 2005, 2009). Specifically the filter that samples O VI is broad compared to conventional narrowband filters, and an extrapolation is required between the continuum-only F140LP filter and F125LP. This extrapolation must be done in the UV, where the continuum shape may vary rapidly as a function of stellar age and dust reddening, and therefore spatially. In regions where the stellar continuum is bright, small errors in the estimated F125LP continuum level may result in significant residual flux (either positive or negative) when the continuum is subtracted. In continuum-bright regions the UV slope or stellar properties may be the best constrained but, counterintuitively, the line flux estimates are in fact the least precise.

The line-flux, F_{line} is calculated from the following expression:

$$F_{\text{line}} = (f_{125} - \zeta_{\text{UV}} \cdot f_{140}) \cdot W_{125} \quad (1)$$

where f_{125} and f_{140} are the f_{λ} flux densities measured in the F125LP and F140LP filters, respectively, and W_{125} is the bandwidth of the F125LP filter. The critical quantity is ζ_{UV} , which is the factor that scales the F140LP flux to estimate the contribution of continuum processes to the F125LP flux. ζ_{UV} is similar to the *Continuum Throughput Normalization* (CTN) factor defined in Hayes et al. (2005, 2009), but is here quoted in flux units without folding in the filter throughput. ζ_{UV} is a single number that captures a lot of physical quantities; to first order it reflects the shape of the UV continuum. This slope is usually parameterized using the functional form of a power-law: $f_{\lambda} \propto \lambda^{\beta}$, where f_{λ} is the continuum flux density per wavelength, which casts β as the (conventionally defined, logarithmic) UV spectral slope. This is governed by stellar age, metallicity, and reddening. Adding complexity, ζ_{UV} may also encode information about discrete features that may fall within the on-line bandpass.

We begin by evaluating the UV slope empirically as a function of position, which we show in Figure 4. We take the images in ACS/SBC/F125LP, F140LP, F150LP, F165LP and WFC3/UVIS/F390W, which span the spectral region between 1160 Å and 3100 Å in the restframe (pivot wavelengths for each filter). Including the weight maps output by `astrodrizzle`, we perform a weighted least-squares fit in every pixel, giving the ‘ β -map’ shown in left panel of Figure 4. This shows that in the central nuclear condensation, the UV slope has a logarithmic gradient of $\beta \approx -1.5$ to -2 , which is consistent with a young, mostly unreddened starburst, although note that this measurement covers a longer wavelength baseline than normally defined. Some regions show β at least as blue as -2.5 at high significance, which is not easy to reproduce with stellar models if all stars are cospatial. For example in some strong starbursts (e.g. Tololo 1247–232; Buat et al. 2002; Puschnig et al in preparation), the UV continuum shortwards of Ly α is too blue to be describable with spectral models, a problem that may be exacerbated when smaller regions are resolved (e.g. at HST resolution). In fainter regions – particularly the northern extended structure – the UV color is much redder and shows β around -0.5 to 0.5 . This is also clearly visible in Figure 5, where the color composite image shows this arm to be much redder than the rest of the galaxy. A ring of pixels showing a UV slope around $\beta = 0$ (flat in f_λ) encompasses the galaxy; most likely this is because the starburst is hosted in an older stellar population.

In this paper we test three methods of estimating ζ_{UV} , which each has advantages and disadvantages. In order of increasing complexity, these are:

A single power-law (SINGLE-PL) — This is the simplest method, in which we adopt a single value for ζ_{UV} across the whole image. We adopt a fiducial value of $\beta = -1.9$, it being the total value computed in a global aperture. This corresponds to $\zeta_{UV} = 1.12$. Adopting a single power law enables us to rapidly explore the limitations due to systematic errors, which we do in Section 5.3.2 using a range of observed β values.

A spatially varying power-law (PIXEL-PL) — As shown in the left panel of Figure 4 the continuum slope is not constant over the whole galaxy, and varies between $\beta = -3.4$ and $\beta = 0$. Assuming the power-law is a complete description of the continuum shape, this corresponds to a range in scale factor, ζ_{UV} , of 1.23 to 1.0. In this method we use the map of ζ_{UV} to subtract a continuum level that varies as a function of position. A key point to note from these Figures is that when the UV slope is *blue* ζ_{UV} is *high*; this results in *more* continuum being subtracted and *less* inferred line emission. Redder slopes would result in more inferred line emission.

A model SED in every pixel (PIXEL-SED) — In reality the UV continuum is not shaped by a single equation but by the properties of stars, gas, and dust; we are therefore concerned that even the PIXEL-PL method is insufficient. To estimate the effects of this we implement a more sophisticated method of extrapolating the continuum into the blue end of the F125LP bandpass using the spectral models. This is the same method we use to subtract the UV continuum from H I Ly α observations in LARS; see Östlin et al. (2014) for the latest description. In short we

perform a stellar SED fit in every pixel, using the *Starburst99* synthetic spectral models (Leitherer et al. 1999, 2014). We adopt a constant stellar metallicity that is closest to the measured nebular value ($Z = 0.004$). Using the five bands of continuum imaging we fit two components of stars, after iteratively subtracting the nebular gas spectrum using the narrowband observations of H α and H β . In each pixel we extrapolate the best-fitting spectrum, convolve it with the F125LP bandpass, and subtract the result from the observation. We note that this method does not perform as well as it does in the LARS project, because the age determination requires the filters to closely bracket the Balmer and 4000 Å spectral breaks. At this redshift the F390W filter is well positioned on the blue side, but the F475W filter is centred at 3900 Å in the restframe, and does not well-sample the red side.

Each method has its own advantages and disadvantages. The SINGLE-PL method allows for very fast tests to be performed, and to estimate the absolute limits of systematic uncertainty. The PIXEL-PL method enables us to account for spatially varying UV colors but exploring the extreme colors is less certain. Neither of the first two methods actually includes any physics, and both assume the continuum behaves as a power-law. The measured values of ζ_{UV} vary by only $\approx 20\%$ (minimum to maximum) across the full image, and the variation is significantly smaller where the UV is well exposed. The PIXEL-SED method allows for realistic shapes of the continuum (e.g. stellar continua and dust reddening do not necessarily behave like power-laws) and may even account for discrete features if the age is constrained precisely enough. However spectral models for O stars are uncertain in the far UV and even more so at metallicities below that of the Magellanic clouds; J1156 has a metallicity around 1/10 the solar value (Asplund et al. 2004). For the PIXEL-SED to perform accurately, the shape of assumed dust-reddening curve must also accurately reflect that of the galaxy.

We are cognizant of the fact that we are trying to measure a line that has a net equivalent width of a few tenths of an Å. The bandpass we use is rather broad at ~ 100 Å, and where the UV continuum is bright and the local EW is low, we do not have the contrast to reliably measure the O VI feature whatever technique we use. However where the continuum is faint and the emission extended, the local EW can become almost arbitrarily high, and if there is little continuum to subtract, then this error is minor and absorption from the continuum is negligible. In such regions the flux will be quite precise, but the local EW will still remain poorly measured.

In this article we present continuum subtractions based upon all three methods. However all of our photometry is based upon the SINGLE-PL method which allows us to estimate the errors per pixel and rapidly quantify both systematic and statistical errors.

We estimate statistical errors with Monte Carlo simulations. We use the `wht` image from `astrodrizzle` and convert it to a standard deviation per pixel. We account for the fact that the drizzling process correlates the noise, and apply the standard average correction (Casertano et al. 2000; Fruchter & Hook 2002). We re-generate the Voronoi cells in the F125LP and F140LP images, and

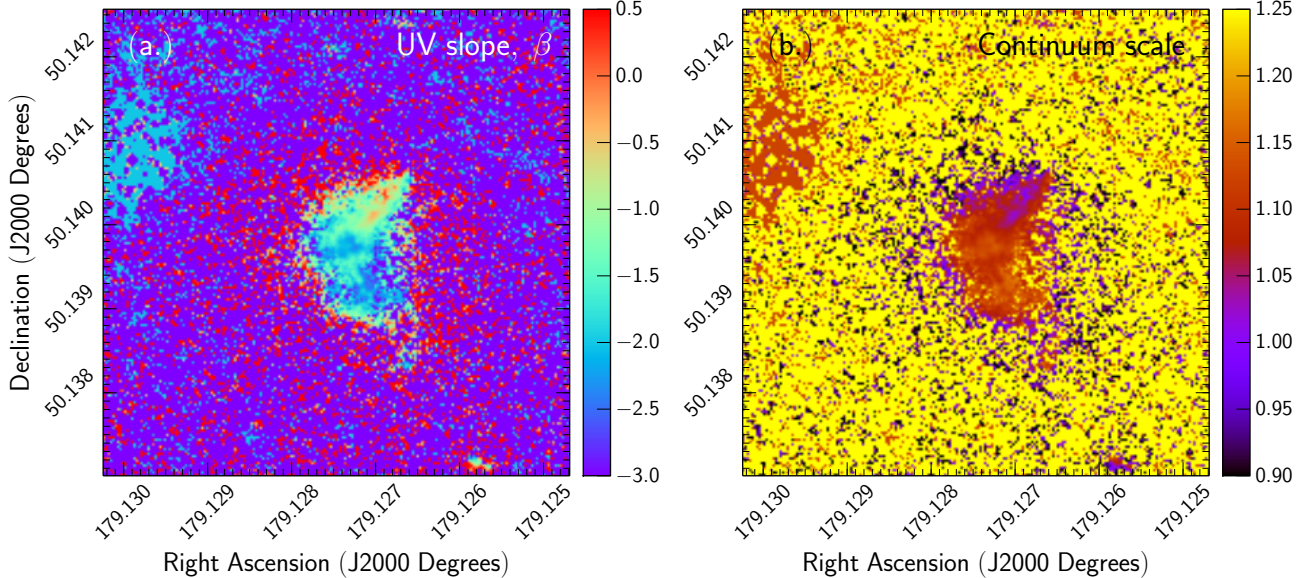


Figure 4. The UV Color of the Stellar Population. *Left* shows the UV continuum slope β , which can be seen to range from as red as 0.5 to as blue as -3 . *Right* shows the corresponding factor by which the offline filter (F140LP) would need to be scaled (in f_λ units) to produce the continuum flux in F125LP for the same β slope, assuming no line emission or absorption in the blue remainder of the bandpass.

perform the same continuum subtraction using the fiducial UV slope of $\beta = -1.9$. We produce 1000 realizations of the O VI image, and for each tessellated cell compute the upper and lower limits that encompass the central 68th percentile ranges of the distribution.

4.2. Spectroscopic Data

Target acquisition with the COS was done in ACQ/IMAGE mode. We first checked that the peak-up process had well centered the galaxy within the Primary Science Aperture (PSA). We examined the header keywords ACQPREFX and ACQPREFY of the `_rawacq` frame, which records the pixel upon which the PSA is centered after the telescope slew. We determine the pixel centering to be just 2 pixels (0.05 arcsec, in a 2.5 arcsec aperture) from the intensity centroid of the brightest condensation in the near ultraviolet acquisition frame.

With the object centered in the aperture, we processed the data using the default settings of the CALCOS pipeline, stopping after spectral extraction and the generation of four `_x1d` files (one for each FP-POS setting). We re-sampled each 1D spectrum onto a common wavelength grid and combined them with the `splice` task in the `stsdas.hst_calib.ctools` package of Pyraf. In this step, unlike the complete run of CALCOS, we more conservatively rejected all spectral pixels that had a non-zero data quality flag. We checked that the geocoronal Ly α and O I line have wavelength centroids that correspond to the vacuum wavelength of the transition; for Ly α they agree to within 0.01 Å (2.5 km s $^{-1}$).

5. DESCRIPTION OF THE RESULTS

The *upper left* panel of Figure 5 shows a color composite of the galaxy, taken in HST optical filters. It has an extremely compact core, just 1 kpc across in the FUV image (*upper right*) that hosts almost all the star-formation. Fitting an exponential profile to the UV continuum gives a scale radius of just ≈ 0.75 kpc, in which the SFR is of the order of 30 M_\odot yr $^{-1}$. The galaxy also shows extended streams indicating that its origin may lie in the

merger of two galaxies.

5.1. O VI Absorption and Emission

Continuum-subtracted F125LP images are shown in the *lower* panels of Figure 5. Figure 6 shows a set of the same continuum-subtracted images, in which we compare the three methods described in Section 4.1.4: SINGLE-PL, PIXEL-PL, and PIXEL-SED. These images also compare the morphology of the continuum-subtracted data when performed on unbinned pixel images and then smoothed, and when Voronoi tessellation is applied. The *lower* panels also include maps of the equivalent width (EW) in the tessellated data only.

The central regions of the galaxy show negative flux. This is expected for observations of strong electronic transitions superposed against bright background continuum sources (as with the absorption line studies discussed in the Introduction), as H I (Ly β) and O VI absorb radiation from the continuum. However, a ring of positive flux is clearly visible surrounding the UV-bright regions of the galaxy. The morphology is not symmetric, and is brighter towards the northwest. In Figure 6, which compares continuum subtractions performed by various methods, we find a close agreement in the flux produced by the SINGLE-PL and PIXEL-PL methods. The PIXEL-SED method, however, produces a bright region emission from the central condensation. The ring-like halo emission, however, shows a similar surface brightness in all methods. The bright central emission is absolutely not supported by the COS spectrum, and this spurious emission arises because the stellar models at this wavelength cannot fully capture the shape of the continuum across the bandpass. We do not consider continuum subtractions made using this method further in this paper. The PIXEL-PL method produces a narrow ring of higher surface brightness than SINGLE-PL, but note also in Figure 6 that the absorbing region is not as wide in the PIXEL-PL subtraction. The equivalent width in such imaging data is particularly hard to measure, as both the emission line and the continuum are faint at radii where the

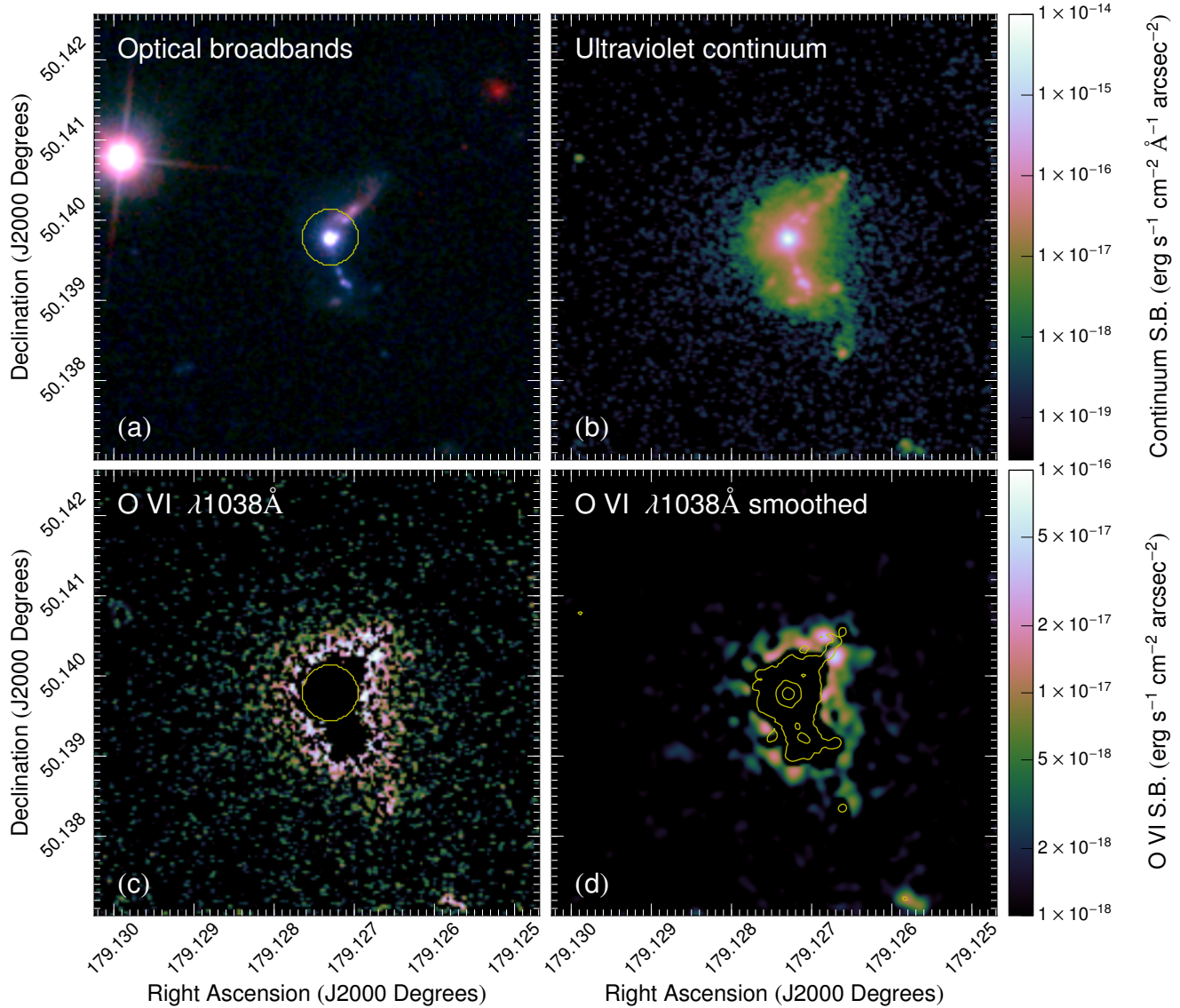


Figure 5. Imaging of J1156. *Upper left:* A color-composite image: the blue channel encodes the F390W filter (restframe 3150 Å), green shows the F475W filter (restframe 3900 Å), and red shows F850LP (restframe 7200 Å). The yellow circle shows the position and size of the spectroscopic aperture. *Upper right:* An ultraviolet continuum image (restframe 1250 Å). *Lower panels:* show the emitted line flux that we interpret to be the O VI $\lambda 1038$ Å emission line. Images use a logarithmic scale. The *left* panel is un-smoothed, and the *right* is smoothed with a Gaussian kernel with $\sigma = 3$ pixels. The yellow contours show UV continuum radiation at levels of 10^{-17} , 10^{-16} , 10^{-15} erg s $^{-1}$ cm $^{-2}$ arcsec $^{-2}$.

O VI emission dominates over Ly β and other absorption. Minor differences in scale factor produce large relative differences in the continuum-subtracted flux, and EWs measured in individual pixel bins are quite uncertain. The main point to read from these EW maps is that the lower values (purple in the color scaling) are found closer to the galaxy, where the continuum is brighter and the high EWs (yellow, red) are found at larger radii. These pixels at large radii, however, are also the most uncertain.

The most likely interpretation of this ring of emission is that the emission comes from the O VI doublet because, very importantly, there are no other strong recombination or collisional lines in the bandpass. The interpretation of O VI emission is supported by a spectrum, obtained in the center, which we show in Figure 7.

The spectrograph has a 2.5-arcsecond diameter circular aperture, which was centered upon the UV dominant star cluster, as illustrated in Figure 5. The spectrum shows saturated absorption in Ly β , and no emission. O VI is also primarily in absorption; the $\lambda 1032$ Å part of the doublet is clearly outflowing, and we measure a blueshift of 380 km s $^{-1}$. The $\lambda 1038$ Å feature is blended with C II $\lambda 1036$ Å absorption, and combined these absorption features confirm the central negative flux seen in Figure 5.

The spectrum shows a weak emission line at restframe $\lambda 1038$ Å, with an integrated flux of $(1.5 \pm 0.6) \times 10^{-16}$ erg s $^{-1}$ cm $^{-2}$. The flux calibration applied by the COS pipeline assumes a point source in the centre of the aperture. This is appropriate for the measured contin-

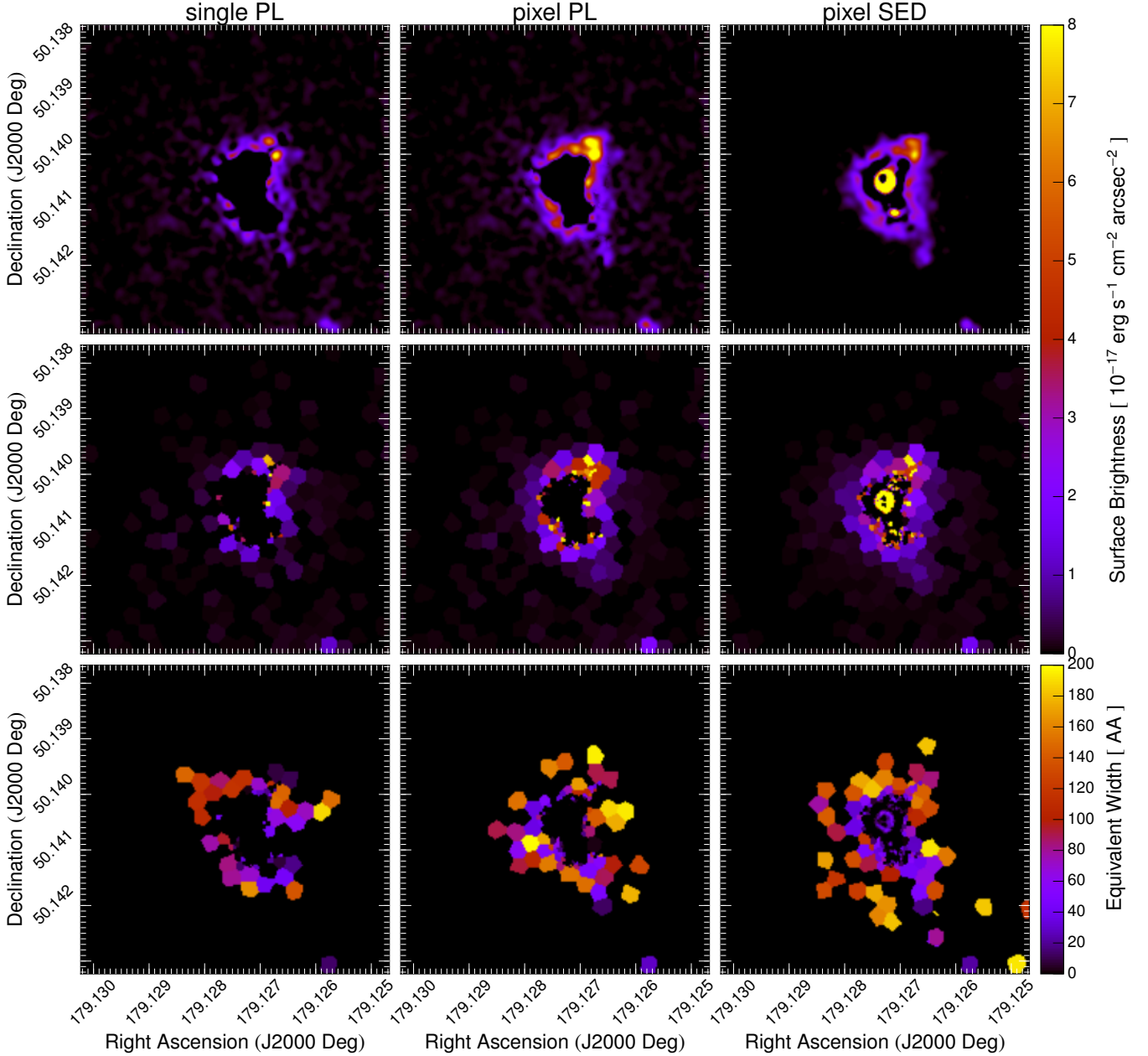


Figure 6. A comparison of the different methods used to subtract the continuum. The *upper* row shows the O VI surface brightness estimated in the unbinned data that have then been smoothed with a 3 pixel Gaussian kernel; the *central* row shows the corresponding surface brightness in the Voronoi tessellated data. The *lower* row shows the O VI equivalent width estimated from the Voronoi tessellated data. Colorbars for each row of Figures are shown to the right. The columns show compare the different methods: *left* shows the SINGLE-PL method, *centre* shows the PIXEL-PL method, and *right* shows the PIXEL-SED method. See text for details.

uum flux which is compact, but the imaging data show the excess line emission to have a shallow surface brightness profile that will be close to constant within the PSA. We apply a 13 % correction for vignetting of the COS aperture⁷.

The $\lambda = 1032 \text{ \AA}$ line in emission is unfortunately absorbed in the H I Ly α transition in the halo of an intervening galaxy at $z = 0.05$, but the blueshifted O VI absorption is still clear and resolved. Further supporting the detection of O VI emission, we also show the averaged spectrum of 20 star-forming galaxies at similar redshift,

which also shows an emission feature in at 1038 \AA . More information on these archival spectra is provided in Section 6.

The lower redshift absorption system is particularly unfortunate because it absorbs any emission from the $\lambda 1032 \text{ \AA}$ part of the doublet. The interloper falls somewhat to the red, but is sufficient to remove the entire feature. Fortunately O VI, as one of the highest ionization potential lines in the UV spectrum, is significantly blueshifted (see, e.g. Grimes et al. 2009) and the 1032 \AA absorption feature is offset from the interloping absorption line. The average blueshift in the local starburst sample observed with FUSE (Grimes et al.

⁷ COS Instrument Handbook Section 5.9.

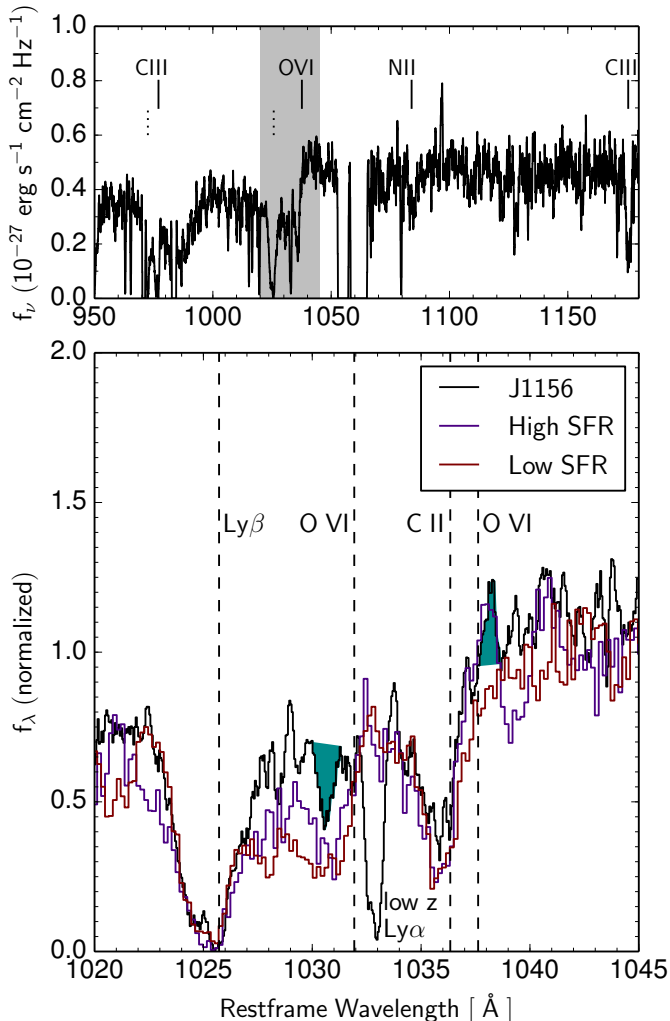


Figure 7. The ultraviolet spectrum around $\text{Ly}\beta$ and O VI . The *upper* panel shows the full spectrum, shifted into the restframe. Strong interstellar metal absorption features are labeled; Lyman lines are shown by vertical dotted lines. The *lower* panel shows the O VI and $\text{Ly}\beta$ region (shaded above) of J1156 in black. Filled patches show the regions identified as the $\lambda 1032 \text{ \AA}$ absorption line (blueshifted) and $\lambda 1038 \text{ \AA}$ emission line. The average spectra of strongly and weakly star-forming galaxies are shown in purple and red, respectively (Heckman et al. 2011; Henry et al. 2015). The spectrum of J1156 and strongly star-forming subsample are remarkably similar and both show a clear O VI emission line at $\lambda 1038 \text{ \AA}$.

2009) is -180 km s^{-1} . In J1156 the SFR is significantly higher, the galaxy more compact, and the outflow velocity is higher: -380 km s^{-1} , and comparable to the maximum in the FUSE sample. A very similar blueshift of $\text{O VI } \lambda 1032 \text{ \AA}$ is seen in the stacked spectra of galaxies with similar SFRs (Section 6 and Figure 11). This blueshift of the $\lambda 1032 \text{ \AA}$ line is particularly fortunate because it enables us to measure the outflow velocity, despite the lower redshift interloper and the blending of the $\lambda 1038 \text{ \AA}$ line with $\text{C II } \lambda 1036 \text{ \AA}$.

The absorption system may, however, cause us to underestimate the O VI column density by lowering the apparent continuum near the O VI line. In this case, our estimate will be a lower limit, but it is worth noting

that J1156 lies well on the observed relationship between N_{OVI} and velocity width, that unifies all O VI absorbing systems from the Milky Way disk to IGM systems (Heckman et al. 2002; Grimes et al. 2009).

We measure the O VI surface brightness from the continuum-subtracted images, using isophotally-defined apertures. This, together with the value measured centrally by COS spectroscopy, is shown in Figure 8. Caution is needed when comparing this surface brightness profile to the images shown in Figures 5 and 6. Pixels are averaged over long annular regions in which the line may be present in either absorption or emission, and the averaging is performed on pixels that do not have the same sign. Thus the annular average may be very much smaller than the peak surface brightness, while the eye is usually guided by the brightest pixels in an image. This is especially true for Figure 5, which is logarithmically scaled and the negative pixels are not displayed. This display issue is common to all profiles nebular lines where the feature can present in both absorption and emission.

The central absorption becomes positive at radii beyond $\approx 2.5 \text{ arcsec}$, corresponding to 9.4 kpc . The central surface brightness is higher than at larger radii, and clearly declines to radii of $\sim 6 \text{ arcsec}$ (23 kpc). We do not attempt to constrain the shape of the surface brightness profile but show that it can be described by an exponential function. We fit the profile using the a simple least-squares minimizer, that gives a central surface brightness $\mu_{\text{OVI}} = (5.3_{-1.1}^{+1.2}) \times 10^{-17} \text{ erg s}^{-1} \text{ cm}^{-2} \text{ arcsec}^{-2}$, with an exponential scale length of $R_{\text{OVI}} = 2.0_{-0.2}^{+0.2} \text{ arcsec}$. In physical distances, this corresponds to $7.5_{-0.7}^{+0.7} \text{ kpc}$. These errors correspond to the 16th and 84th percentiles, determined by Monte Carlo simulations of the original science frames, which were randomized using their corresponding weight images; continuum subtractions and profile fits were computed for each realization. Integrating this profile to infinity gives a total O VI flux of $(12.3_{-0.7}^{+1.1}) \times 10^{-16} \text{ erg s}^{-1} \text{ cm}^{-2}$ and a luminosity of $(20.5_{-1.2}^{+1.8}) \times 10^{40} \text{ erg s}^{-1}$. Because this measures only the $\lambda 1038 \text{ \AA}$ part of the doublet, the total O VI output may be $\sim 2-3$ times higher (Grimes et al. 2007). These numbers are summarized in Table 3, which we will continue to populate throughout the following Sections.

5.2. Recombination Line Emission

In Figure 9 we show the continuum subtracted $\text{Ly}\alpha$ and $\text{H}\alpha$ images, together with O VI . Note that different intensity ranges are used in each panel and, as the Figure shows, the peak $\text{Ly}\alpha$ surface brightness is on the order of 100 times that of O VI . Due to the significantly shorter integration times in the $\text{Ly}\alpha$ and $\text{H}\alpha$ filters, we are not able to probe the same regions that we can in O VI : the F125LP image (O VI) has over 20 times the exposure time of F150LP ($\text{Ly}\alpha$) and also has around twice the peak throughput (Figure 3). The radial profiles of $\text{Ly}\alpha$ and $\text{H}\alpha$, together with that of O VI , are shown in Figure 10. As we cannot compare line fluxes at large radii, we instead measure the corresponding exponential scale lengths in $\text{H}\alpha$ and $\text{Ly}\alpha$. In practice it is difficult to obtain a robust result because of the very compact nature of the starburst. For $\text{H}\alpha$ we obtain an exponential scale length of 0.2 arcsec (0.75 kpc) and $\sim 0.3 \text{ arcsec}$ (1.1 kpc)

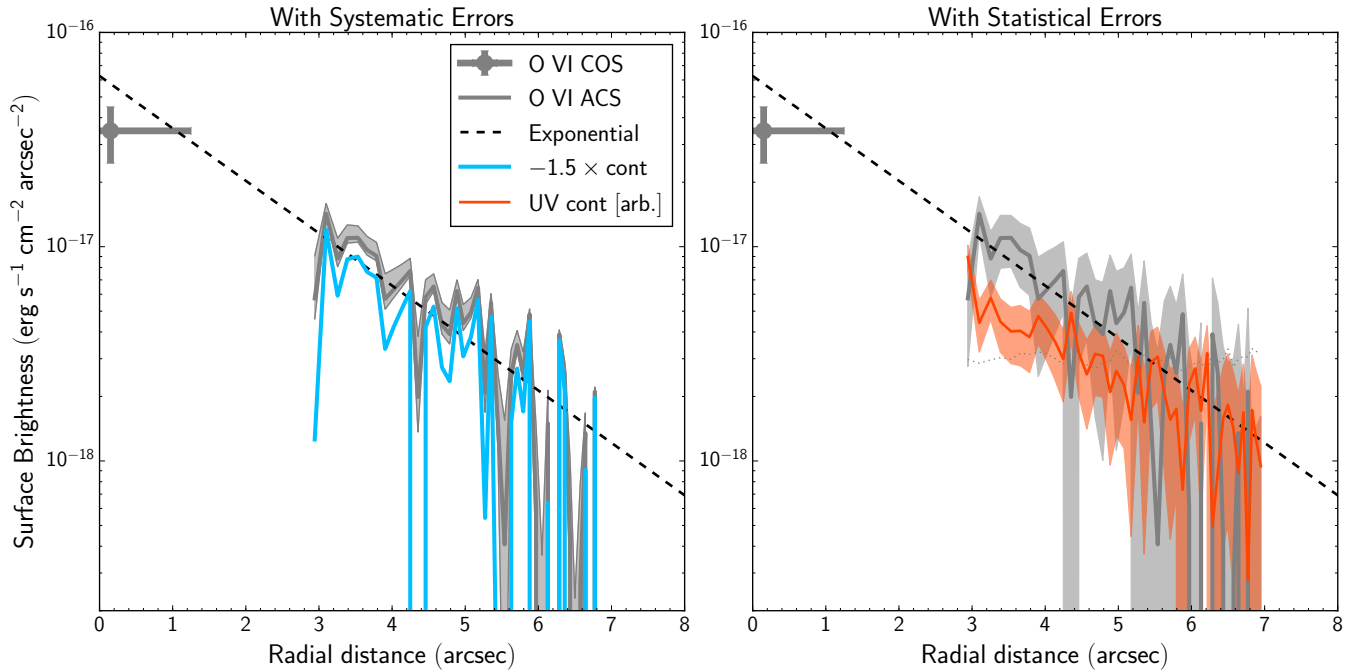


Figure 8. The O VI surface brightness profile. The gray point at radius ≈ 0.1 arcsec is the spectroscopic measurement, slightly offset for visibility, with x-errorbar showing the radius of the aperture. The line beginning at radius ~ 2.5 arcsec shows the surface brightness measured in the images in isophotal apertures. Due to the logarithmic scaling, and the fact that more flux is absorbed in total (mainly in Ly β) only flux beyond ~ 2 arcsec can be visualized. The dashed black line shows the best-fitting exponential profile. Shaded regions show the estimated systematic error budget from varying the slope of the UV continuum (*left*) and upper and lower limits of the 68th percentile statistical errors from Monte Carlo simulations (*right*). The *right* panel also shows the profile of the UV continuum radiation.

for Ly α , where the error is about 0.1 arcsec. These scale lengths are $\sim 1/10$ and $\sim 1/7$ that of the O VI profile.

Interestingly the Ly α /H α ratio is high: aperture flux growth curves of Ly α and H α converge at fluxes of 1.1×10^{-13} and 3.7×10^{-14} erg s $^{-1}$ cm $^{-2}$, respectively. With a Ly α luminosity of 1.8×10^{43} erg s $^{-1}$, J1156 is the most luminous known Ly α -emitting galaxy at $z < 0.8$ (Cowie et al. 2011; Hayes et al. 2014; Henry et al. 2015; Hayes 2015, c.f. Wold et al. 2014). A Ly α /H α ratio of ≈ 2.9 is precisely what is expected for pure dust attenuation using the measured H α /H β ratio – there is little room for significant preferential absorption of Ly α because of a large number of resonance scatterings.

5.3. Is the halo O VI?

Having isolated a potential flux excess in the on-line filter, we must now solidly address two questions: *is the excess flux real and significant?* and, if so, *is it a halo of O VI emission?*

5.3.1. Instrumental and Methodological Effects

Turning first to the question of the reality, the most obvious and important issues are those of instrumental effects such as residual dark current, red leaks in the filters, and the point spread function (PSF) or scattered light. ACS/SBC indeed does have a significant dark current that is centrally peaked. However the dark current is strongly temperature dependent: below ≈ 25 degrees Celsius the dark current is slightly below 10^{-5} counts sec $^{-1}$ px $^{-1}$, while above this temperature it grows substantially. From a cold start the SBC reaches this temperature after ≈ 3 hours of operating time, which corresponds to about two orbits. As discussed in Section 3.2.1, we firstly divided our 16 orbits of F125LP

and F140LP observations into eight visits of two orbits, and secondly arranged with STScI for our visits to be executed only when the SBC has not been used in the previous 24 hour period. According to the current status of the SBC, the dark current should not be detectable in any of our images. Moreover, we arranged the exposures within our visits such the F125LP frames are interleaved between the F140LP in the same orbit, using shadow time for F125LP. Thus, even if there were some residual dark current in the frames it should be well balanced between the two exposures.

The PSF wings of the SBC are particularly broad, and a mis-match between the F125LP and F140LP filters could mimic such a halo. Measuring the PSF at large radii, and at a wavelength where the majority of stars are very faint, is extremely challenging. We have made a major effort to characterize the wings of the SBC PSF in the relevant filters, used here and in the LARS project (Melinder et al. in preparation). The method and main results can be found in Appendix A of this article and a much more general study of the HST PSFs is in preparation. In short we obtained data of white dwarf stars in the globular cluster NGC 6681, drizzled and stacked the images in each filter. We then identified all the UV sources in the stacked image, and selected the 20 brightest stars from which to build an empirical PSF. We extracted stamps of the individual stars, normalized and stacked them. To combat contamination from nearby sources, we then used this 2-dimensional PSF to remove all objects apart from one from the drizzled image, and thus produced 20 images containing only one of the 20 reference stars in each. We then repeated the extraction, stacking, and removal three times until the empirical PSF converged. This procedure enabled us

Table 3
Derived Properties of O VI and Gas in the Coronal Phase.

Quantity (1)	Symbol used (2)	O VI (3)	Coronal (4)	Unit (5)
Imaging				
Central Surface Brightness	μ_{OVI}	$5.3^{+1.2}_{-1.1} \times 10^{-17}$...	$\text{erg s}^{-1} \text{cm}^{-2} \text{arcsec}^{-2}$
Angular scale length	R_{OVI}	2.0 ± 0.2	...	arcsec
Physical scale length	R_{OVI}	7.5 ± 0.7	...	kpc
Total flux	f_{OVI}	$12.3^{+1.1}_{-0.7} \times 10^{-16}$...	$\text{erg s}^{-1} \text{cm}^{-2}$
Total luminosity	L_{OVI}	$20.5^{+1.8}_{-1.2} \times 10^{40}$...	erg s^{-1}
Spectroscopy				
Column density	N_{OVI}	$10^{14.7}$	$10^{19.2}$	cm^{-2}
Outflow velocity	V_{OVI}	380	...	km s^{-1}
Combination				
Density	n	1.7×10^{-05}	0.50	cm^{-3}
Column length of clouds	D_{OVI}	10	...	pc
Gas mass	M_{OVI}	3×10^4	5.5×10^7	M_{\odot}
Cooling time	t_{cool}	1.3	...	Myr
Sound crossing time	t_{sound}	10^4	...	yr
Total kinetic energy	E_K	3.2×10^{52}	5.9×10^{55}	erg
Momentum		1.7×10^{45}	3.1×10^{48}	g cm s^{-1}
Pressure	p	...	1.6×10^5	K cm^{-3}

Note. — Column (1) lists the quantity, and (2) the symbol used in the Paper. Column (3) presents the measured value where appropriate for O VI. Column (4) presents, where appropriate, the same quantity but converted into a corresponding value for the mostly hydrogen gas that is assumed to be in CIE with the O VI. The Table is divided by horizontal lines into quantities that are derived from imaging, spectroscopy, and the combination of the two.

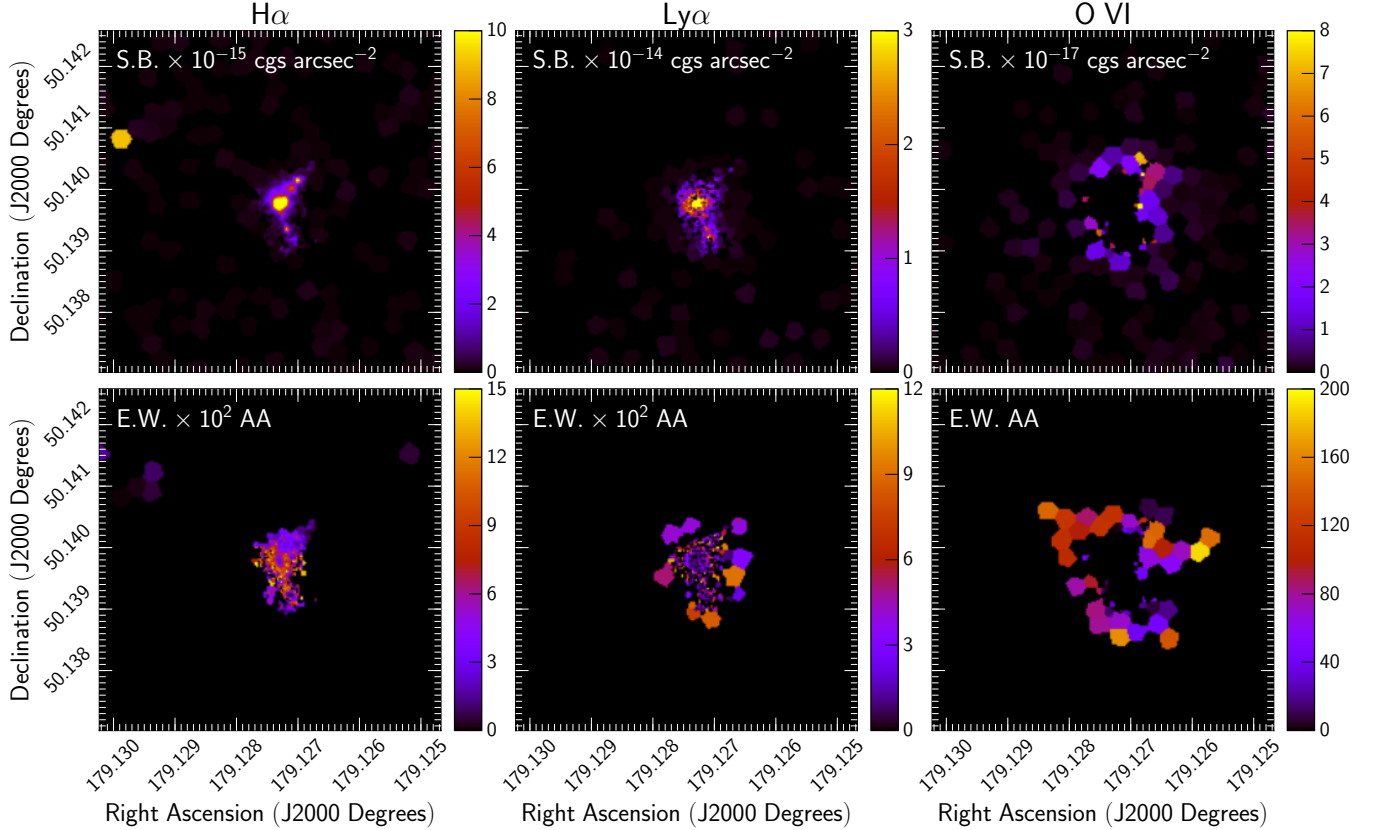


Figure 9. J1156 in various continuum-subtracted emission lines. *Left* shows H α , *centre* shows Ly α , and *right* shows O VI. Here we present the Voronoi tessellated data. Surface brightness levels in $\text{erg s}^{-1} \text{cm}^{-2} \text{arcsec}^{-2}$, and are different in each panel, each of which has its own color-bar.

to measure the PSF wings of F125LP and F140LP out to radii of 3 arcsec, which we show to be indistinguishable at these distances. We begin to see halo emission in the continuum-subtracted image at radii somewhat smaller

than this, and even if J1156 were a point source, PSF wings would not be able to explain the halo. Since the galaxy is not point-like, PSF issues or scattered light may not explain the detection, although we cannot rule out

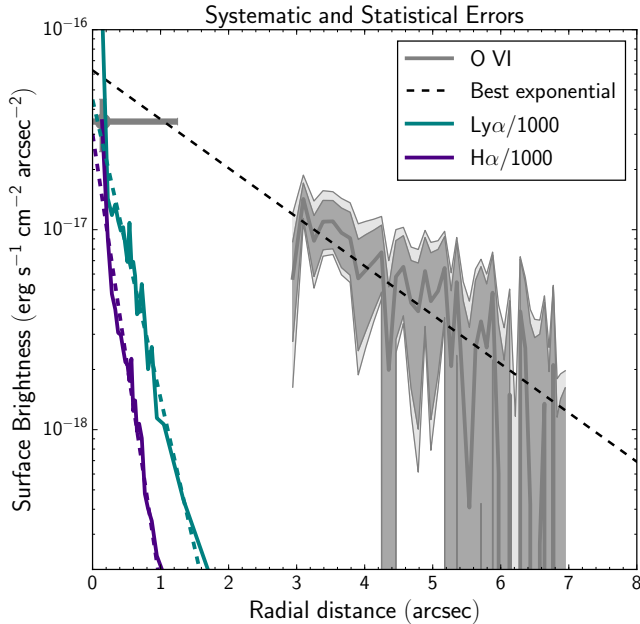


Figure 10. The same as Figure 8 except the systematic and statistical errors have been combined. Here we also add the radial profiles of Ly α (cyan) and H α (blue) in order to compare with emission that comes purely from photoionization. Ly α and H α profiles have been divided by 1000 to be included in the same Figure.

minor effects on the photometry at larger radii still.

5.3.2. Significance of the Detection

Next arises the question of how significant the detection is. This depends upon an accurate understanding of the noise characteristics, the treatment of the reduced frames, and the continuum subtraction.

As described in Section 4.1.4, we execute Monte Carlo simulations to determine the significance of the detection. Since we drizzle the pixels from a fine sampling (0.034") to a coarser one (0.1"), noise correlation from individual pixels will be minor, but account for it formally nonetheless (Casertano et al. 2000; Fruchter & Hook 2002). Our Monte Carlo simulations are conducted end-to-end, and the random numbers that are drawn are used only to re-realize the science frames. All subsequent calculations are carried out using the original method in resampled data, and in the surface brightness profile (*right* panel of Figure 8) each pixel error contributes precisely once per realization. At radii between 2.5 and ≈ 4.5 " the annular SNR is around 3 on average; this radial range includes 41 spatial elements, and if summed only in this region gives a total SNR of 21. Note that this SNR is around a factor of 2 larger than that quoted for the integrated flux (Table 3) when the surface brightness profile is integrated to infinity. The reason for this is the large extrapolation in radius. The relative error becomes larger beyond ~ 5 arcsec, and rapidly the signal becomes indistinguishable from the noise. Statistical errors, while obviously important, cannot explain our detection.

As suggested in Section 4.1.4, we have performed the continuum subtraction based upon a single assumption for the UV continuum slope ($\beta = -1.9$), but we also adopt a range of $-3.4 < \beta < 0$ to explore systematic errors. β of -3.4 is far bluer than stellar models can reproduce, but is the largest value measured in the β -map.

Stellar populations can become arbitrarily red, especially in the UV, but our lower value corresponds to a slope that is flat in f_λ .

These limiting surface brightness profiles are shown by the gray error region in the left panel of Figure 8. It is true that stellar continuum slopes can become somewhat redder but they cannot become bluer. Were our assumed slope too red we would over-predict the line emission, but in adopting -3.4 as the limiting case this is the most pessimistic continuum subtraction we can envisage, with $\zeta_{UV} \approx 1.2$. The key point in assessing O VI surface brightness is that redder slopes will only result in more O VI. This point is particularly important: Figure 4 shows that the continuum is rather red in the regions where the O VI emission is seen: if the O VI were the result of significantly extended PSF wings in F125LP we would infer a blue slope in these regions, not redder. This cannot affect the detection of excess flux.

While the approach assumes a parametric form of the slope, this encompasses all feasible variations in stellar metallicity, stellar age, segregation of low and high mass stars, and reddening by dust. It is clear from Figure 8 that while the UV stellar continuum does affect the O VI surface brightness, the detection itself cannot arise artificially from a poor estimate of the UV slope. Finally, we execute tests where we artificially multiply the offline filter by completely unrealistic ζ_{UV} factors (2, 3, and 5 were tested) and still the result is an excess flux in the O VI image. As the right panel of the same Figure shows, the statistical errors actually far outweigh the systematic ones.

5.3.3. Sources of the Emission

Having argued that the excess flux is real line emission we must establish that it is indeed O VI, because other absorption, and potential emission features fall within the bandpass. The Ly β line will be intrinsically 1/3 the strength of Ly α under Case A conditions: Ly α is shown in Figures 9 and 10 and is hundreds of times brighter than O VI. When Ly α is emitted by local starbursts, it is almost ubiquitously with the morphology of large halos (e.g. Hayes et al. 2013) due to scattering in atomic hydrogen. Ly β may also scatter in H I, but at each event the probability of a $^3P_{1/2} \rightarrow ^1S_{1/2}$ Ly β transition is around 4/5, while the remaining 1/5 is a decay to the $^2S_{1/2}$ level resulting in H α , then two-photon, emission. Thus while Ly α can scatter indefinitely, Ly β may do so only a handful of times. We may expect Ly β in principle to be emitted if it can escape directly from the central regions, but any halo should not be as extended as Ly α , and in realistic circumstances would exhibit a steeper profile, if seen at all. Since we do not see a Ly β line in the centre of the galaxy, and the Ly α profile declines far more steeply than the suspected O VI halo, we do not believe our halo is one of scattered Ly β . Moreover the entire FUSE archive of starbursts (Grimes et al. 2009), and more recent COS observations of similar galaxies (e.g. Heckman et al. 2011; Henry et al. 2015, see also Section 6), do not present convincing cases for Ly β emission, and we anyway do not believe the Case A scenario needed for Ly β . O VI on the other hand has, albeit rarely, been seen in emission.

The C II $\lambda 1036 \text{ \AA}$ feature is also a resonance line and therefore scatters as well as absorbs, and may also repro-

cess radiation into a fluorescent emission line (C II*) with wavelength 1037.0 Å. This fluorescent line, if present, is 190 km s⁻¹ bluewards of the O VI λ1038 Å line, and indeed a small peak is visible in the spectrum which could possibly be C II*. If so, however, this is around 1/5 the strength of the line we have identified as O VI λ1038 Å, and is therefore unlikely to be the emission we see at large R .

After eliminating Lyβ, scattered C II, and fluorescent C II* emission, we conclude that the excess emission in the F125LP filter arises from the O VI transition at 1038 Å. However we do not know whether it is due to gas that is collisionally ionized (or even photoionized) in situ, or whether it is continuum radiation that is resonantly scattered by O VI ions. Indeed if there is gas there to be emitting because of collisional ionization, it must also be scattering. This was discussed in Grimes et al. (2007), who pointed out that in Haro 11 the emitted O VI was of roughly equal EW to the absorbed line, which would be expected for scattering. Examining the COS spectrum of J1156 – which samples a similar physical scale to the FUSE in Haro 11 (see Section 8) – the situation appears to be very similar. However the emitting region in the images that we interpret as O VI extends over a far greater area than that covered by the COS aperture, and when the exponential profile is integrated to infinity the luminosity is about eight times higher than in the COS aperture alone: 2.5×10^{40} c.f. 2.0×10^{41} erg s⁻¹, as further discussed in Section 8. In contrast, more than 80 % of the UV continuum flux, measured in F140LP, comes from within the COS aperture. For a spherically symmetric case a component of the emission must be due to scattered continuum radiation, but we estimate that this mechanism contributes only $\approx 1/6$ of the total halo emission. Of course a departure from spherical symmetry – for example if we are looking into a lower-than-average column of coronal gas – will increase the scattered component. Currently there is no obvious way to estimating this for J1156.

In summary, we believe that while the signal is weak in general, we have detections of O VI in both imaging and spectroscopic mode. The signal is far above the noise based upon both statistical and systematic error budgets, and the available spectroscopic information suggest that O VI 1038 Å is the most likely feature. We argue that only a minority of the measured emission should be due to resonance scattering. Furthermore, a very similar feature is visible in stacked spectra of archival observations, which we review in the next Section.

6. SPECTRA AROUND O VI FOR AN ENSEMBLE OF STARBURSTS

We searched the MAST archive for COS/G130M observations of starburst galaxies with redshifts that place the O VI doublet in the wavelength region covered by the grating ($z = 0.12 - 0.4$). Two main studies dominate this archive search, one targeting the nearby analogues of Lyman Break Galaxies – so-called Lyman Break Analogs (GO 11727 and GO 13017; PI: T. Heckman) – and one targeting Green Pea galaxies (GO 12928; PI: A. Henry). These galaxies are summarized in Table 4. Spectra were obtained and processed in an identical manner as for J1156, as described in Section 4.2.

To examine the O VI feature in an ensemble of galax-

ies, we averaged the spectra in a number of sub-samples. We first measured the systemic redshifts by obtaining the SDSS spectrum, and measuring the wavelength centroid of the Hα, Hβ, and [O III] λλ4959, 5007 Å lines. We converted each to a redshift and took the unweighted average for each galaxy. We then produced a mask for each object to exclude wavelength regions where the continuum is affected by interstellar absorption lines (in both the Milky Way and the target galaxy) and stellar features (in the target galaxy only). We fitted a low order polynomial function to each spectrum and normalized each one. We then blueshifted each spectrum into the restframe using the redshift obtained from nebular lines. With the spectra normalized and shifted into the restframe, we finally masked the Milky Way absorption features in each spectrum and computed a simple average. We produced stacks for the full sample of 20 galaxies, and also for subsamples by dividing the sample in two halves when sorted by Hα both luminosity and equivalent width.

The average properties of the galaxies in the stacks are presented in Table 5 and the resulting spectra are shown in Figure 11. We briefly compare the observables of J1156 with those of the stacked samples. J1156 has a Hα luminosity of 3.3×10^{42} erg s⁻¹ (SFR = 26 M_⊙ yr⁻¹; Kennicutt 1998). This is marginally higher than the most strongly star-forming galaxy in the archival sample (25 M_⊙ yr⁻¹). The high $W_{H\alpha}$ stack has $W_{H\alpha}$ in the range 375–1094 Å, while J1156 shows $W_{H\alpha}$ of 370 Å, and would thus be the median galaxy if included in the stack.

We first compare the intensely star-forming subsamples with their more weakly star-forming counterparts in the *left* panel of Figure 11. The absorption regions of the spectrum appear broadly similar. This is true particularly for Lyβ, is true also for the blended C II λ1036 Å and O VI λ1038 Å lines, and to a lesser extent holds for the O VI λ1032 Å feature. The most striking difference that emerges when intensely star-forming galaxies are isolated in the stack is the presence of an emission feature at $\lambda \approx 1038$ Å that does not appear in the stacks of less star-forming galaxies. In the less star-forming galaxies the continuum rolls more smoothly into the absorption feature without discrete feature.

We have investigated the possibility that the apparent increased strength of the 1038 Å emission may instead result from stronger O I 1039 Å absorption, that produces a spurious emission feature. The archival spectra also extend to redder wavelengths and include the O I 1302 Å electric dipole transition. These two O I features arise from the same lower energy level and the two lines are expected to covary. In fact, the transition probability for 1302 Å is ≈ 7 times higher and we can therefore use it as a test of what to expect at 1039 Å. Unlike at 1039 Å, the 1302 Å line is clearly visible in all sub-stacks, and we measure EWs in the range 0.86–1.12 Å. Indeed the absorption is slightly stronger in the higher SFR sub-stacks, but the relative difference is only ≈ 25 %. Typical errors in EW are around 0.2 Å, and this difference is barely significant. Moreover even if the trend were to hold the magnitude is too small to explain the difference at 1039 Å. Given that the 1302 Å lines are present in all stacked spectra, we do not believe the 1038 Å emission feature arises purely from increased O I absorption

Table 4
Archival galaxies used in the stacking analysis.

SDSS ID	RA J2000	Dec J2000	Redshift	Prog. ID	$L_{\text{H}\alpha}$ $10^{42} \text{erg s}^{-1}$	$W_{\text{H}\alpha}$ \AA
(1)	(2)	(3)	(4)	(5)	(6)	(7)
J005527.46-002148.7	00:55:27.5	-00:21:48.7	0.16742	11727	1.76	379.2
J015028.4+130858.3	01:50:28.4	+13:08:58.3	0.14667	11727	1.03	200.6
J030321.41-075923.2	03:03:21.4	-07:59:23.2	0.16481	12928	1.18	589.8
J091113.34+183108.1	09:11:13.3	+18:31:08.1	0.26217	12928	1.90	390.3
J092159.38+450912.3	09:21:59.4	+45:09:12.3	0.23497	11727	1.08	74.24
J092600.4+442736.1	09:26:00.4	+44:27:36.1	0.18067	11727	1.41	578.0
J105330.82+523752.8	10:53:30.8	+52:37:52.8	0.25260	12928	2.50	375.6
J111244.05+550347.1	11:12:44.0	+55:03:47.1	0.13163	13017	1.43	205.8
J111323.99+293039.2	11:13:23.9	+29:30:39.2	0.17514	13017	0.104	26.30
J113303.78+651341.3	11:33:03.8	+65:13:41.3	0.24141	12928	0.649	277.1
J113722.13+352426.6	11:37:22.1	+35:24:26.6	0.19431	12928	2.03	562.8
J114422.31+401221.2	11:44:22.3	+40:12:21.2	0.12695	13017	0.443	87.38
J121903.98+152608.5	12:19:04.0	+15:26:08.5	0.19558	12928	1.63	1094
J124423.37+021540.4	12:44:23.4	+02:15:40.4	0.23938	12928	3.15	777.5
J124834.63+123402.9	12:48:34.6	+12:34:02.9	0.26341	12928	1.64	669.5
J141612.96+122340.5	14:16:12.9	+12:23:40.5	0.12316	13017	1.11	184.5
J142405.72+421646.2	14:24:05.7	+42:16:46.2	0.18482	12928	2.14	1083
J142856.4+165339.4	14:28:56.4	+16:53:39.4	0.18167	13017	1.39	251.2
J161245.59+081701	16:12:45.5	+08:17:01.0	0.14914	13017	1.62	175.4
J210358.74-072802.3	21:03:58.8	-07:28:02.3	0.13677	11727	1.95	107.3
J115630.63+500822.1	11:56:30.4	+50:08:28.0	0.23599	13656	3.32	369.4

Note. — Galaxies are ordered by right ascension. J1156 is not included in the stacking analysis but is included for comparative purposes in the last row.

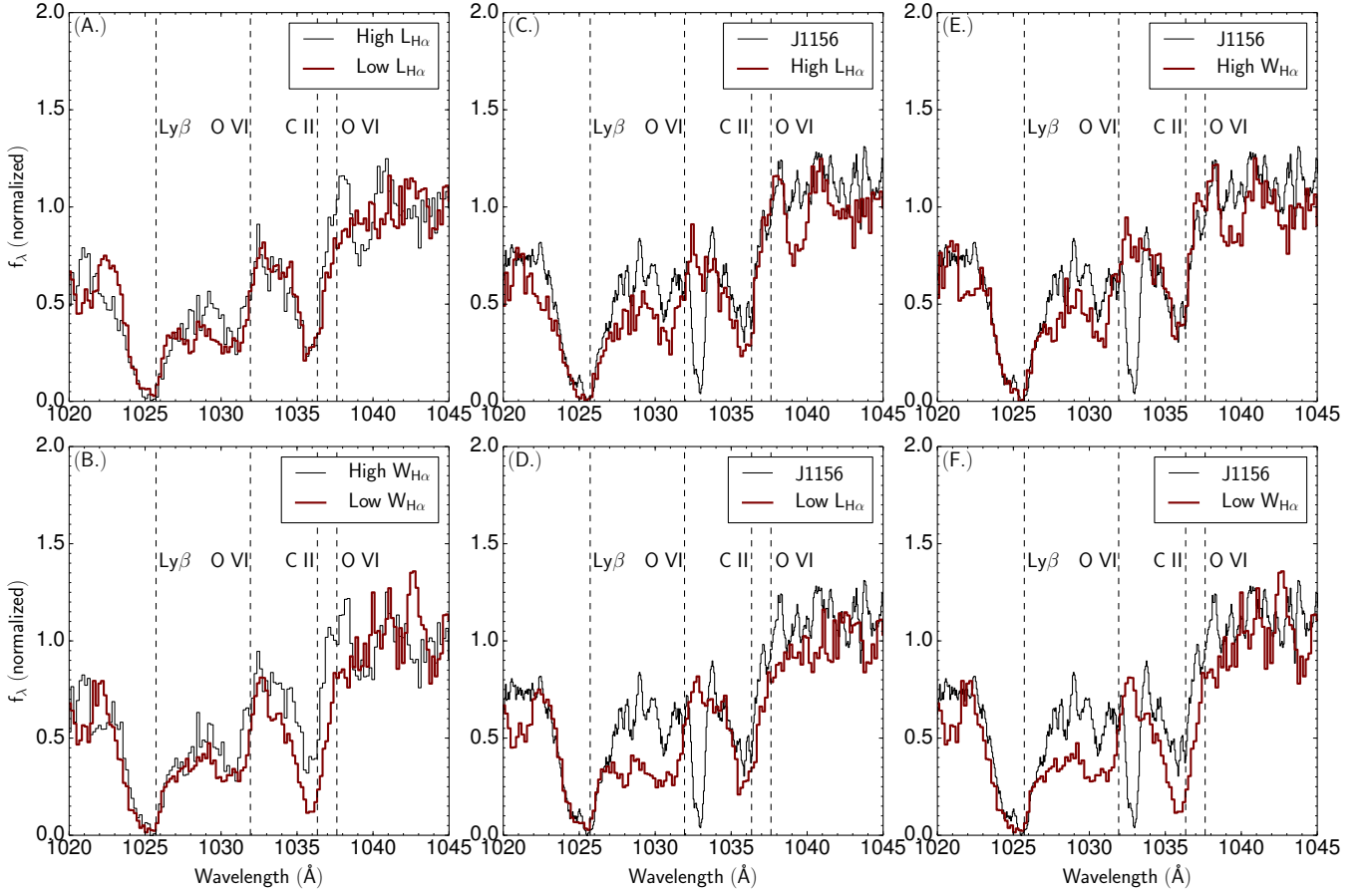


Figure 11. The Differential Stacking Analysis. The *left* panels show the comparison of the higher and lower $L_{\text{H}\alpha}$ subsamples (*upper*), and the higher and lower $W_{\text{H}\alpha}$ subsamples (*lower*). The *central* and *right* panels compare the high/low $L_{\text{H}\alpha}/W_{\text{H}\alpha}$ subsamples with J1156. The wavelengths of $\text{Ly}\beta$, $\text{C II } \lambda 1036 \text{ \AA}$, and the O VI doublet are marked.

at 1039 \AA , and the most straightforward interpretation is that the peak is O VI emission in the higher SFR and

higher $W_{H\alpha}$ galaxies.

The *centre* and *right* panels of Figure 11 show the comparison of the J1156 spectrum with stacks of the low and high $L_{H\alpha}$ and $W_{H\alpha}$ subsamples. Both of the intensely star-forming stacks show remarkable similarity to J1156. For example, the shape and offset of the $Ly\beta$ are almost indistinguishable between J1156 and the average of 10 starbursts. Similarly the C II $\lambda 1036$ Å cannot easily be separated by eye. Most importantly, and as in the previous paragraph, the O VI $\lambda 1038$ Å feature appears similar to the stacked spectra in the two strongly star-forming cases: it forms at the same rest wavelength with a similar equivalent width (as well as EW can be measured). Note that it is possible that both emission and absorption lines are likely to appear artificially broadened in a stacking analysis, as they may not be formed at precisely the same velocity, compared to the optical line emission. The comparison supports a scenario in which strongly star-forming galaxies produce a weak emission feature in their spectrum at the wavelength where O VI would be expected, and where an excess is seen in J1156.

7. INTERPRETING THE O VI FEATURES

Absorption line studies can target O VI at much larger radial distances than imaging can, and have been performed out to distances of 300 kpc (Prochaska et al. 2011). The *COS-Halos* study has revealed two relevant correlations: (a.) the decrease of O VI column density (N_{OVI}) with increasing impact factor; (b.) the increase in N_{OVI} with star formation intensity. However these samples contain only two star-forming galaxies with quasars sightlines inside the 23 kpc over which we see emission. Our study probes much smaller distances, in a galaxy that is forming stars 20 times more intensely than the strongest in *COS-Halos*. We regard the imaging data to be highly complementary to halo spectroscopy in that it provides two-dimensional mapping and probes gas nearer the star-forming region. Indeed relying upon high volume density for emission, this is likely to be the only gas that O VI imaging will be sensitive to. In the following Sections we derive some physical properties of the halo gas that we observe, including its density, mass, how it was excited, and what its fate will be.

At the end of Section 5.3.3 we discussed the possibility that some of the halo emission could be scattered in the O VI transition and not be due to collisional processes. We estimated that in a spherically symmetric situation only $\sim 1/6$ of the observed O VI would be due to scattering, but acknowledge that departure from spherical symmetry could lead to a larger scattered contribution. We assume that collisional processes dominate in the calculations that follow, but note that the derived numbers are accurate only in the case that the scattered contribution is relatively minor.

7.1. Physical conditions in the O VI-bearing gas

We calculate (or place constraints upon) some of the main physical conditions in the O VI gas. Using the apparent optical depth method (Savage & Sembach 1991; Sembach et al. 2003) and the O VI $\lambda 1032$ Å absorption line, we determine the column density of O VI ions to be $\log(N_{\text{OVI}}/\text{cm}^{-2}) \approx 14.7$ along the line of sight to the central star-forming cluster. The error on this value is about

40 %, which dominates the error on all subsequent calculations. In the same measurement we obtain a FWHM of 220 km s^{-1} ; this corresponds to a Doppler parameter $b(= \sigma\sqrt{2})$ of 132 km s^{-1} , and the galaxy lies perfectly among the starbursting population in the $N_{\text{OVI}}-b$ diagram in Grimes et al. (2009). This diagram, when populated with O VI absorbing systems from the plane of the Milky Way, galaxy disks, and IGM clouds has been used by Heckman et al. (2002) to conclude that all O VI absorbing systems have a common physical origin: that they are cooling flows as they pass through the $T \sim 10^{5.5}$ K phase.

Assuming the O VI gas we see in absorption is the same as in emission, we may use the measured column density and a few motivated assumptions to predict the surface brightness in emission. To compute the emission we need the normalized cooling rate, $\Lambda_n n_e^2$, and the electron density n_e , where the cooling coefficient is normally calculated at the solar oxygen abundance (e.g. Sutherland & Dopita 1993). When scaled by the gas metallicity, these give us the volumetric cooling rate Λ , in units of $\text{erg s}^{-1} \text{ cm}^{-3}$. With a dimension of luminosities per volume, we may compute the expected surface brightness if we know the optical length, D_{OVI} – the physical “thickness” of the emitting and absorbing gas along the line-of-sight. That is:

$$\mu_{\text{OVI}} = \Lambda_n n_e^2 \left(\frac{Z}{Z_\odot} \right) D_{\text{OVI}} \quad (2)$$

where μ_{OVI} is the O VI surface brightness and we have introduced Z/Z_\odot to scale down the emissivity for less metallic plasma. While we do not know n_e or D_{OVI} , they are not independent and are related through the column density by $n_e = N_{\text{OVI}}/[D_{\text{OVI}}(\text{O}/\text{H})]$, where (O/H) is the number of oxygen particle per proton that is in equilibrium with the O VI. If we insert this into Equation 2 and equate μ_{OVI} to the observed central surface brightness $\mu_{\text{OVI},0}^{\text{obs}}$ measured in Section 5.1, we can solve for D_{OVI} and obtain:

$$D_{\text{OVI}} = 2\Lambda_n \left(\frac{N_{\text{OVI}}}{\text{O}/\text{H}} \right)^2 \left(\frac{Z}{Z_\odot} \right) \frac{1}{\mu_{\text{OVI},0}} \quad (3)$$

The factor 2 arises because of the assumption of spherical symmetry where we integrate over the full column and not the half column from which the column density is measured (there is as much gas behind the cluster as in front). Note also that two metallicity-like quantities enter here: the (O/H) scales the measured O VI column density to N_e , and the (Z/Z_\odot) scales the cooling function to the metallicity of the galaxy. Cancelling one (O/H) would introduce additional factors.

We assume the gas is in collisional ionization equilibrium (CIE). We appreciate that the gas could in principle be photoionized (e.g. Tripp et al. 2008) we motivate the CIE assumption by (a.) the relative values of N_{OVI} and the absorption line width b , following Heckman et al. (2002), and (b.) the fact that the O VI surface brightness profile is ten times more extended than that of $H\alpha$, which is almost certainly photoionized. While the propagation of ionizing photons to these distances cannot be ruled out, photoionization to O VII would require 138 eV photons and the radiation field would also be rich with

Table 5
Statistics for the Subsamples.

Subsample	Statistic	Redshift	$L_{\text{H}\alpha}$ $10^{42} \text{erg s}^{-1}$	$W_{\text{H}\alpha}$ \AA	SFR($\text{H}\alpha$) $M_{\odot} \text{yr}^{-1}$
(1)	(2)	(3)	(4)	(5)	(6)
Full	Mean	0.18763	1.51	404.5	11.9
	Median	0.18117	1.53	326.4	12.1
	Minimum	0.12316	0.10	26.30	0.82
	Maximum	0.26341	3.15	1094	24.9
High $L_{\text{H}\alpha}$	Mean	0.20456	2.03	561.5	16.1
	Median	0.19495	1.93	476.6	15.2
	Minimum	0.13677	1.62	107.3	12.8
	Maximum	0.26341	3.15	1094	24.9
Low $L_{\text{H}\alpha}$	Mean	0.17071	0.983	247.5	7.77
	Median	0.16998	1.09	203.2	8.66
	Minimum	0.12316	0.104	26.30	0.82
	Maximum	0.24141	1.43	589.8	11.3
High $W_{\text{H}\alpha}$	Mean	0.21052	1.93	650.0	15.3
	Median	0.19495	1.83	583.9	14.5
	Minimum	0.16481	1.18	375.6	9.33
	Maximum	0.26341	3.15	1094	24.9
Low $W_{\text{H}\alpha}$	Mean	0.16475	1.08	159.0	8.54
	Median	0.14791	1.10	180.0	8.66
	Minimum	0.12316	0.104	26.30	0.82
	Maximum	0.24141	1.95	277.1	15.4

Note. — SFRs are lower limits, as they assume no obscuration of $\text{H}\alpha$.

H I-ionizing radiation as well. No strong He II emission line is seen in the optical at 4686 \AA . For the normalized cooling coefficient in CIE we adopt that of Bertone et al. (2010), which is computed for solar metallicity: $\log(\Lambda/n_e^2[\text{erg s}^{-1} \text{cm}^{-3}]) = -22.5$. For the metallicity we use a value of $12 + \log(\text{O}/\text{H}) = 7.87$, which we derived from the temperature-sensitive method in Section 2.

The resulting O VI column length is $D_{\text{OVI}} = 10 \text{ pc}$. We compare D_{OVI} to the exponential scale length of the O VI emitting surface (7.5 kpc; Figure 8): assuming spherical symmetry and that the absorbing and emitting gas are cospatial and uniformly fill the spectroscopic aperture, the gas must be strongly clumped, occupying $\approx 1/750$ of the volume along the line-of-sight (D_{OVI} divided by the exponential scale length).

A narrow O VI emitting region – thin with respect to the galaxy halo – is to be expected if the $T \approx 10^{5.5} \text{ K}$ regions represent shocked gas. Heckman et al. (2001) present hydrodynamical simulations that aim to interpret the O VI absorption in NGC 1705, showing O VI to arise only in the hydrodynamical interaction between hot, out-rushing gas: their Figure 4 is particularly illustrative in this context, as it shows only the O VI phase, and would represent a tiny fraction of the size of the object over most sightlines.

The unique combination of emission and absorption observations outlined above enable us also to derive the electron density in the coronal phase, giving $n_e = 0.50 \text{ cm}^{-3}$. From this we may also derive the thermal pressure, for which we obtain $P/k_B \approx 1.6 \times 10^5 \text{ K cm}^{-3}$, where k_B is Boltzmann’s constant. At this point we note the similarity between this number and the value derived in the nebular phase from the ratio of components in the [S II] doublet: the ratio of the $6717/6731 \text{ \AA}$ [S II] lines actually falls slightly above the low-density asymptotic value in the electron density the curve (Osterbrock 1989), where the minimum density is $\approx 4.65 \text{ cm}^{-3}$. However at 1σ our upper limit on the density is 44 cm^{-3} . From

these measurements we obtain best value for the pressure in the nebular regions of $P/k_B \approx 6.8 \times 10^4 \text{ K cm}^{-3}$, with $65.4 \times 10^4 \text{ K cm}^{-3}$ as the upper limit. This range of pressures closely brackets that measured in the coronal phase, and raises the question of whether the coronal gas and H II regions could be in pressure equilibrium.

If the clouds are not confined by external pressure then they will disrupt on a few sound crossing times. From these characteristics of the coronal phase and the physical thickness of the clouds reported above, we can calculate the minimum sound crossing time, which is $\approx 10^4$ years. The computed crossing time is two orders of magnitude smaller than the cooling time (derived in the following subsection), and if they were not confined by external pressure the clouds would likely be dispersed before they are visible through their own emission. Thus it seems plausible that the two gas phases are indeed in pressure equilibrium, although we must admit that the similarity in P/k_B could be coincidental. If a causal connection is correct, we could be seeing the effects of gas clouds being pressurized from the outside by the volume-filling hot gas that would be seen at X-ray energies.

In NGC 1705, Heckman et al. (2001) compute temperatures and pressures in the O VI phase, under the assumption that the [S II]-derived electron density can be applied to the coronal phase. In J1156 we find tentative support for this correspondence, using independent estimates in the warm gas. The calculations above are quite approximate, but one should note that the number of assumptions is actually rather small. The metallicity cannot be modified by large factors, and no ionization correction has (yet) entered the calculation because we have so far only only concerned ourselves with the electrons in collisional equilibrium with the O VI. Indeed the largest assumption is that the gas is in CIE (Oppenheimer et al. 2016).

7.2. Mass, Energy, and Momentum in the Coronal Phase

If we assume that the radial decline in O VI surface brightness is purely a consequence of the geometrically decreasing column density, then we may compute the total number of O VI ions in the halo. This follows from taking the central O VI column density and the scale length, and integrating the exponential profile to infinity. This calculation places just $3 \times 10^4 M_\odot$ in oxygen at $T \approx 10^{5.5}$ K, and $5.5 \times 10^7 M_\odot$ in the coronal phase in CIE with the O VI.

We may also compute the nebular gas mass as

$$M_{\text{ion}} = \frac{\mu m_p n_p L_{\text{H}\beta,0}}{h\nu_{\text{H}\beta} n_e \alpha_{\text{H}\beta}^{\text{eff}}} \quad (4)$$

where μ is the mean molecular weight, m_p and n_p are the mass and number density of protons, $L_{\text{H}\beta,0}$ is the intrinsic H β luminosity corrected for dust reddening with $H\alpha/H\beta$, h is Planck's constant, $\nu_{\text{H}\beta}$ is the frequency of H β , and $\alpha_{\text{H}\beta}^{\text{eff}}$ is the Case B recombination coefficient for H β . Adopting $\mu = 0.5$ for a pure electron-proton gas, $n_e = 4.65 \text{ cm}^{-3}$ from the [S II] doublet, and $\alpha_{\text{H}\beta}^{\text{eff}} = 2 \times 10^{-14} \text{ cm}^3 \text{ s}^{-1}$ (Osterbrock 1989, for $T \approx 15,000\text{K}$), we compute $M_{\text{ion}} \approx 2.5 \times 10^9 M_\odot$. The corresponding mass in oxygen is $1.3 \times 10^6 M_\odot$. For the O VI mass quoted above, there is 45 times as much mass in the nebular phase as there is in the coronal.

If we assume that all of the coronal gas is moving at the characteristic outflow velocity measured from the O VI $\lambda 1032 \text{ \AA}$ line, we can compute the kinetic energy and momentum in the coronal gas. The kinetic energy in O VI ions alone is $3.2 \times 10^{52} \text{ erg}$, and $5.9 \times 10^{55} \text{ erg}$ in the whole coronal phase of the wind. The momentum in the O VI ions is $1.7 \times 10^{45} \text{ g cm s}^{-1}$, and $3.1 \times 10^{48} \text{ g cm s}^{-1}$ in the whole coronal phase of the wind.

We may also estimate the total mechanical energy that has been returned to the ISM by feedback from star formation. In Section 2 we performed SED fitting to constrain the age of the stellar population, arriving at a best-fitting age of 11.5 Myr, with a 1σ range of 10–39 Myr. In the same calculation, the most frequently recovered star-formation history was an exponentially declining SFR with e -folding time of just 5 Myr. With the age so close to the characteristic SFR decay time, constraining the true SFH between limits of instantaneous and constant is close to impossible. The H α EW also places some constraints: a value of 370 \AA is compatible with a lower limit on the age of just 4.5 Myr (Leitherer et al. 1999) in the case of an instantaneous burst. Taking the best-fitting values of age=11.5 Myr, stellar mass of $1.5 \times 10^9 M_\odot$, the total mechanical energy budget, summing over O star winds and supernova ejecta, is $7.8 \times 10^{57} \text{ erg}$. While these numbers carry a large number of uncertainties and model-dependencies, we calculate that $\sim 1\%$ of the total available mechanical energy is to be found in the kinetic energy of the current coronal outflow. How much *should* be in this phase at any given time depends upon how long-lived the O VI phase is, which we address in the next Section.

7.3. The Fate of the Coronal Gas

In the previous subsection we derived the cooling rate of the gas, Λ . Having also obtained n_e we may also compute the internal energy U , and the ratio U/Λ therefore

gives the cooling time, $t_{\text{cool}} = 1.3 \text{ Myr}$. This corresponds to a mass cooling rate of $42 M_\odot \text{ yr}^{-1}$ (almost identical to the SFR) and a cooling distance of 0.5 kpc at the outflow velocity of 380 km s^{-1} . Thus it is clear that the $10^{5.5}$ K gas cannot have traveled far at this temperature and certainly cannot have been lifted to the scale height from the nuclear star-forming regions. Instead the coronal phase must be constantly replenished.

The stellar mass of J1156 is $1.5 \times 10^9 M_\odot$; at the scale height of 7.5 kpc the escape velocity v_{esc} , assuming only the mass in stars, is $\approx 38.6 \text{ km s}^{-1}$. Thus if stars were the only mass available to bind the wind, the average velocity would be ten times the escape velocity. Given that $v_{\text{esc}} \propto \sqrt{M}$, the dark matter mass inside of 7.5 kpc must exceed 100 times the stellar mass in order to prevent the wind from escaping. The halo abundance-matching analysis of Moster et al. (2013) suggests that a galaxy of $M_{\text{stell}} = 1.5 \times 10^9 M_\odot$ will have a dark matter halo mass of $\approx 10^{11} M_\odot$. Assuming the dark matter density profile to be isothermal, v_{esc} is approximately 3 times the maximum halo rotation velocity, v_{circ} (e.g. Weiner et al. 2009). Maller & Bullock (2004) have shown that for a halo mass of $10^{11} M_\odot$, $v_{\text{circ}} \approx 65 \text{ km s}^{-1}$. The corresponding v_{esc} is 200 km s^{-1} , and the conclusion that the coronal gas is becoming unbound appears robust assuming that no additional energy is drained from the wind.

Even if the current outflow velocity exceeds the escape velocity, it does not necessarily imply that the gas will escape as energy losses from radiation could play a significant role in the future of the outflow. Indeed the cooling distance is just half a kpc, so the gas cools almost in situ. We calculate that $\sim 1\%$ of the available mechanical energy is accounted for in the coronal outflow, and the remainder is either still available in the piston gas, will have cooled already, or was radiated immediately without ever contributing to the wind fluid. Assuming a constant O VI luminosity with time, $7.4 \times 10^{55} \text{ erg}$ have been radiated in O VI over the 11.5 Myr duration of the star formation episode. This is remarkably close to the current kinetic energy in the wind ($5.9 \times 10^{55} \text{ erg}$, above) but compared to the $7.8 \times 10^{57} \text{ erg}$ returned by supernovae and O stars, this is a minor loss of energy compared to the total amount that has been available.

The amount of energy that is truly available in the wind is that supplied directly to the piston gas, which is not simply the sum of the mechanical energy returned from stellar winds and SNe. The mechanical energy in this $T \sim 10^{7.8}$ K wind fluid is dependent upon the thermalization efficiency of the SN ejecta, commonly denoted ϵ , which is not known in this case (or many cases). Strickland & Heckman (2009) derive $0.3 < \epsilon < 1$ for nearby starburst M82, but some simulations suggest that early radiative losses in the densest cores of strong nuclear starbursts may reduce ϵ to below 0.1 (Thornton et al. 1998; Stevens & Hartwell 2003). Even if we were to adopt $\epsilon = 0.1$, then only around one tenth of the energy budget would have been radiated through the O VI emission line. X-ray observations would be particularly useful in determining the total energy budget.

If the gas is ejected from the galaxy, the metals will no longer contribute to the metal abundance of J1156. However for the calculated cooling time the gas will have cooled and recombined within $\approx 1 \text{ Myr}$ and within just

0.5 kpc. Hence even if it does escape, this gas will be easily detectable through H I Ly α absorption and transitions of O I in the ultraviolet.

8. COMPARISON WITH OTHER DETECTIONS OF O VI EMISSION

Finally we compare our J1156 observations with the other two known O VI-emitting galaxies that were observed with the FUSE: NGC 4631 (Otte et al. 2003) and Haro 11 (Grimes et al. 2007). First, however, a brief description of the different nature of these observations is warranted. COS and FUSE are both aperture spectrographs, but have very different entrance windows: the PSA of COS is a circular aperture with a diameter of 2.5 arcsec, while FUSE sampled a square of 30 arcsec on the side. However the fact that the targeted galaxies lie at very different distances almost entirely compensates for this. J1156 and the stacked sample discussed in this paper reside at $z \approx 0.24$ and $\langle z \rangle = 0.19$, respectively (≈ 1 Gpc). At these distances, the COS aperture samples 9.4 kpc in J1156 and 7.9 kpc in the archival sample.

Haro 11 lies at 84 Mpc, which is just 1/12 the distance of our COS samples, and the larger FUSE aperture still subtends 12 kpc (full diameter). This is just 25 % larger than the physical size sampled by COS in J1156. For Haro 11 the FUSE aperture captures the entirety of the UV continuum. The O VI $\lambda 1038$ Å flux in the FUSE aperture is $(1.4 \pm 0.5) \times 10^{-14}$ erg s $^{-1}$ cm $^{-2}$, which corresponds to a luminosity of 1.26×10^{40} erg s $^{-1}$. The $\lambda 1038$ Å flux of J1156, measured in the COS aperture alone, gives a luminosity of 2.5×10^{40} erg s $^{-1}$ – note that this refers to the COS aperture only, and is not the luminosity integrated to infinity quoted in Table 3. Thus the O VI luminosity of J1156 is within a factor of two that of Haro 11. Given the very similar natures of the galaxies, and the $\sim 3\sigma$ detections obtained in both cases, these are very similar. In fact, simply scaling the luminosities by the SFRs of the galaxies would completely reconcile the luminosities. When we integrate the exponential surface brightness profile to infinity we obtain a luminosity of 2×10^{41} erg s $^{-1}$, which is eight times higher than measured in the COS aperture. Haro 11 is also a particularly compact galaxy, and we may speculate that the aperture losses may be similar. Note again the FUSE aperture did not allow Grimes et al. (2007) to distinguish between collisional ionization and scattering, and it is unfortunate that Haro 11 is too low redshift to be observed with our imaging method.

NGC 4631 is a much more regular edge-on disk galaxy, and is also significantly nearer, at a distance of just 7.5 Mpc (J1156 is 160 times more distant). At this distance FUSE samples just 1.1 kpc. NGC 4631 was observed on two pointings, that targeted an extra-planar X-ray bubble. Pointing A was obtained at a disk scale height of 4.8 kpc, while B was positioned 2.5 kpc above the disk. This type of observation is advantageous because observing away from the disk reduces contamination from a noisy UV continuum where absorption may blend with emission. We obtained the FUSE spectra of NGC 4631 from the MAST archive (Program ID: P134; PI: E. Murphy), and re-measured the O VI emission. Correcting for Milky Way extinction, we measure 5.2×10^{-18} erg s $^{-1}$ cm $^{-2}$ arcsec $^{-2}$ (position A) and 6.7×10^{-18} erg s $^{-1}$ cm $^{-2}$ arcsec $^{-2}$ (position B). Our ob-

servations are barely sensitive such surface brightnesses, but at similar radial distances J1156 is significantly brighter in O VI. However NGC 4631 forms stars at just $\sim 1 M_{\odot}$ yr $^{-1}$, which is ~ 40 times lower than J1156 (~ 20 times lower than Haro 11), and over a significantly more extended disk. Thus we would very much expect the O VI surface brightness to be lower.

9. SUMMARY AND CONCLUSIONS

We have used the *Hubble Space Telescope* to image a star-forming galaxy in nine filters between the far ultraviolet and z -band, enabling us to produce high spatial resolution images in four emission lines: the O VI doublet at $\lambda\lambda = 1032, 1038$ Å, and the Ly α , H α , and H β lines of H I. We detect O VI in emission. While not the first detection of O VI emission from a starburst galaxy, this is the first time the line emission has been spatially resolved and mapped. The O VI emission takes the form of a very extended halo; the surface brightness profile can be described by an exponential function, with scale length of 7.5 kpc. This is 10 times the scale length of the nebular ionized gas measured by H α , and the continuum radiation from massive stars (measured using the far UV continuum). We detect O VI emission out to radii of 23 kpc. Integrating the light profile to infinity we obtain the first O VI luminosity of a galaxy at any redshift: $(20.5^{+1.8}_{-1.2}) \times 10^{40}$ erg s $^{-1}$.

Ultraviolet spectroscopy obtained on the central pointing confirms O VI emission, and also reveals the absorption component of the transition. By contrasting the absorbed flux with the halo emission we estimate that about 1/6 the total luminosity can arise (assuming spherical symmetry) due to stellar continuum radiation being resonantly scattered by O VI ions in the halo. The UV spectrum enables us to measure the column density of O VI ions, which is $\log(N_{\text{OVI}}/\text{cm}^{-2}) \approx 14.7$. By assuming collisional ionization equilibrium and the measured oxygen abundance, we can compute the expected surface brightness in emission for a given physical thickness of the O VI region; equating this with the observed surface brightness we solve for the size of the O VI region along the line-of-sight, which is just 10 pc. The scale length of emission is 750 times this distance, implying the $T \approx 10^{5.5}$ K gas must be very clumpy, or, very roughly, fills just $\sim 10^{-3}$ of the volume. This is consistent with – and indeed expected of – O VI being produced at the hydrodynamical interfaces of hotter outflowing gas where it collides with and compresses against denser, cold circumgalactic gas (e.g. Heckman et al. 2001, 2002).

From these calculations we derive the electron density in the coronal phase to be 0.5 cm^{-3} . A pressure of $P/k_{\text{B}} \approx 1.6 \times 10^5 \text{ K cm}^{-3}$ follows from the temperature and density, and we compare this to the pressure of the H II regions that is independently derived from the [S II] doublet in the SDSS spectrum. The pressures in the two phases agree within the $1 - \sigma$ level. Our calculations also include the derivation of both the cooling time ($\approx 10^6$ yr) and the sound crossing time ($\approx 10^4$ yr). From these two points we speculate that the pressure agreement may be causal, and that both phases exist in pressure equilibrium with the hotter phase that drives the outflow and fills the volume. Indeed the disruption timescale for the estimated cloud sizes (a few sound-crossing times) is so short compared to the cooling time that this pressure

confinement may be a requirement to see the O VI gas in emission at all.

Assuming that the decreasing surface brightness with radius is due to a geometrical decrease in the column length, and therefore the column density (i.e. the volume density is constant), we compute the mass of O VI ions to be $3 \times 10^4 M_{\odot}$. Assuming the nebular metallicity is equivalent to that of the H II regions, we obtain a total mass of gas at $T \approx 300,000$ K to be $5.5 \times 10^7 M_{\odot}$. This is just $\sim 2\%$ of the mass in the ionized ISM.

We calculate the current, instantaneous kinetic energy of the coronal phase of the wind to be 5.9×10^{55} erg. Comparably, 7.4×10^{55} ergs have been radiated in O VI over the whole estimated lifetime of the starburst. This however, is just $\sim 1\%$ of the 7.8×10^{57} erg in mechanical energy that has been returned to the ISM by the collective winds from massive stars and the ejecta from core-collapse supernovae. Thus even if the thermalization efficiency is low, it is likely that the coronal phase contains a small fraction of the available energy and mass at any given time. Even over the lifetime of the star formation episode, the radiative loss of wind energy through the O VI lines must be small.

The O VI absorbing gas, measured in the spectrum, is shown to be outflowing with an average velocity of 380 km s^{-1} . We compute the expected escape velocity, which we determine to be significantly smaller than the speed of the outflowing gas. If the coronal gas is becoming unbound, then the metals entrained in the outflow will no longer contribute to the metallicity of the galaxy, and will instead enrich the local intergalactic medium. However given the short cooling time and cooling length of just 0.5 kpc, the gas will have cooled and recombined before escaping. These baryons will therefore become visible to Lyman series absorption studies and the oxygen will be visible to O I absorption (e.g. at 1302 \AA).

We are grateful to Emily Freeland, Joop Schaye, Arjan Bik, and Daniela Calzetti for useful discussion regarding this, and followup work. We thank the referee for providing insightful feedback that greatly strengthened the manuscript. M.H. acknowledges the support of the Swedish Research Council (Vetenskapsrådet) and the Swedish National Space Board (SNSB), and is Fellow of the Knut and Alice Wallenberg Foundation.

Facilities: HST (ACS,WFC3,COS).

REFERENCES

- Ahn, C. P., Alexandroff, R., Allende Prieto, C., et al. 2014, *ApJS*, 211, 17
- Andrews, B. H., & Martini, P. 2013, *ApJ*, 765, 140
- Asplund, M., Grevesse, N., Sauval, A. J., Allende Prieto, C., & Kiselman, D. 2004, *A&A*, 417, 751
- Becker, A. C., Homrighausen, D., Connolly, A. J., et al. 2012, *MNRAS*, 425, 1341
- Beirão, P., Armus, L., Lehnert, M. D., et al. 2015, *MNRAS*, 451, 2640
- Benson, A. J., Bower, R. G., Frenk, C. S., et al. 2003, *ApJ*, 599, 38
- Bergvall, N., Zackrisson, E., Andersson, B.-G., et al. 2006, *A&A*, 448, 513
- Bertone, S., Schaye, J., Booth, C. M., et al. 2010, *MNRAS*, 408, 1120
- Bolzonella, M., Miralles, J.-M., & Pelló, R. 2000, *A&A*, 363, 476
- Bouché, N., Lehnert, M. D., & Péroux, C. 2005, *MNRAS*, 364, 319
- Braun, H., & Schmidt, W. 2012, *MNRAS*, 421, 1838
- Bregman, J. N. 2007, *ARA&A*, 45, 221
- Bruzual, G., & Charlot, S. 2003, *MNRAS*, 344, 1000
- Buat, V., Burgarella, D., Deharveng, J. M., & Kunth, D. 2002, *A&A*, 393, 33
- Calzetti, D., Armus, L., Bohlin, R. C., et al. 2000, *ApJ*, 533, 682
- Cappellari, M., & Copin, Y. 2003, *MNRAS*, 342, 345
- Casertano, S., de Mello, D., Dickinson, M., et al. 2000, *AJ*, 120, 2747
- Cen, R., & Ostriker, J. P. 2006, *ApJ*, 650, 560
- Chevalier, R. A., & Clegg, A. W. 1985, *Nature*, 317, 44
- Chisholm, J., Tremonti, C. A., Leitherer, C., et al. 2015, *ApJ*, 811, 149
- Chung, J., Rey, S.-C., Sung, E.-C., et al. 2013, *ApJ*, 767, L15
- Cowie, L. L., Barger, A. J., & Hu, E. M. 2011, *ApJ*, 738, 136
- Danforth, C. W., Shull, J. M., Rosenberg, J. L., & Stocke, J. T. 2006, *ApJ*, 640, 716
- Diehl, S., & Statler, T. S. 2006, *MNRAS*, 368, 497
- Efstathiou, G. 2000, *MNRAS*, 317, 697
- Erb, D. K., Quider, A. M., Henry, A. L., & Martin, C. L. 2012, *ApJ*, 759, 26
- Feruglio, C., Fiore, F., Carniani, S., et al. 2015, *A&A*, 583, A99
- Fruchter, A. S., & Hook, R. N. 2002, *PASP*, 114, 144
- Grimes, J. P., Heckman, T., Strickland, D., et al. 2007, *ApJ*, 668, 891
- Grimes, J. P., Heckman, T., Aloisi, A., et al. 2009, *ApJS*, 181, 272
- Hayes, M. 2015, *PASA*, 32, 27
- Hayes, M., Östlin, G., Mas-Hesse, J. M., & Kunth, D. 2009, *AJ*, 138, 911
- Hayes, M., Östlin, G., Mas-Hesse, J. M., et al. 2005, *A&A*, 438, 71
- Hayes, M., Östlin, G., Schaerer, D., et al. 2013, *ApJ*, 765, L27
- Hayes, M., Östlin, G., Duval, F., et al. 2014, *ApJ*, 782, 6
- Heckman, T. M. 2002, in *Astronomical Society of the Pacific Conference Series*, Vol. 254, *Extragalactic Gas at Low Redshift*, ed. J. S. Mulchaey & J. T. Stocke, 292
- Heckman, T. M., Alexandroff, R. M., Borthakur, S., Overzier, R., & Leitherer, C. 2015, *ApJ*, 809, 147
- Heckman, T. M., Armus, L., & Miley, G. K. 1990, *ApJS*, 74, 833
- Heckman, T. M., Norman, C. A., Strickland, D. K., & Sembach, K. R. 2002, *ApJ*, 577, 691
- Heckman, T. M., Sembach, K. R., Meurer, G. R., et al. 2001, *ApJ*, 554, 1021
- Heckman, T. M., Borthakur, S., Overzier, R., et al. 2011, *ApJ*, 730, 5
- Henry, A., Scarlata, C., Martin, C. L., & Erb, D. 2015, *ApJ*, 809, 19
- Hoopes, C. G., Sembach, K. R., Howk, J. C., Savage, B. D., & Fullerton, A. W. 2002, *ApJ*, 569, 233
- Hopkins, P. F., Quataert, E., & Murray, N. 2012, *MNRAS*, 421, 3488
- Kennicutt, Jr., R. C. 1998, *ARA&A*, 36, 189
- Kornei, K. A., Shapley, A. E., Martin, C. L., et al. 2012, *ApJ*, 758, 135
- Leitherer, C., Ekström, S., Meynet, G., et al. 2014, *ApJS*, 212, 14
- Leitherer, C., Schaerer, D., Goldader, J. D., et al. 1999, *ApJS*, 123, 3
- Maller, A. H., & Bullock, J. S. 2004, *MNRAS*, 355, 694
- Martin, C. L. 2005, *ApJ*, 621, 227
- McKee, C. F., & Ostriker, J. P. 1977, *ApJ*, 218, 148
- Moster, B. P., Naab, T., & White, S. D. M. 2013, *MNRAS*, 428, 3121
- Murray, N., Quataert, E., & Thompson, T. A. 2005, *ApJ*, 618, 569
- Oke, J. B., & Gunn, J. E. 1983, *ApJ*, 266, 713
- Oppenheimer, B. D., Crain, R. A., Schaye, J., et al. 2016, *ArXiv e-prints*, arXiv:1603.05984
- Osterbrock, D. E. 1989, *Astrophysics of gaseous nebulae and active galactic nuclei*
- Östlin, G., Marquart, T., Cumming, R. J., et al. 2015, *A&A*, 583, A55
- Östlin, G., Hayes, M., Duval, F., et al. 2014, *ApJ*, 797, 11
- Otte, B., Murphy, E. M., Howk, J. C., et al. 2003, *ApJ*, 591, 821
- Peeples, M. S., Werk, J. K., Tumlinson, J., et al. 2014, *ApJ*, 786, 54

- Postman, M., Brown, T., Sembach, K., et al. 2010, in Society of Photo-Optical Instrumentation Engineers (SPIE) Conference Series, Vol. 7731, Society of Photo-Optical Instrumentation Engineers (SPIE) Conference Series, 77312K
- Prochaska, J. X., Gawiser, E., Wolfe, A. M., Castro, S., & Djorgovski, S. G. 2003, *ApJ*, 595, L9
- Prochaska, J. X., Weiner, B., Chen, H.-W., Mulchaey, J., & Cooksey, K. 2011, *ApJ*, 740, 91
- Prochaska, J. X., Weiner, B. J., Chen, H.-W., & Mulchaey, J. S. 2006, *ApJ*, 643, 680
- Reddy, N. A., & Steidel, C. C. 2009, *ApJ*, 692, 778
- Rivera-Thorsen, T. E., Hayes, M., Östlin, G., et al. 2015, *ApJ*, 805, 14
- Rubin, K. H. R., Prochaska, J. X., Koo, D. C., et al. 2014, *ApJ*, 794, 156
- Rubin, K. H. R., Weiner, B. J., Koo, D. C., et al. 2010, *ApJ*, 719, 1503
- Rupke, D. S., Veilleux, S., & Sanders, D. B. 2005, *ApJS*, 160, 115
- Savage, B. D., Kim, T.-S., Wakker, B. P., et al. 2014, *ApJS*, 212, 8
- Savage, B. D., Narayanan, A., Lehner, N., & Wakker, B. P. 2011, *ApJ*, 731, 14
- Savage, B. D., & Sembach, K. R. 1991, *ApJ*, 379, 245
- Sembach, K. R., Tripp, T. M., Savage, B. D., & Richter, P. 2004, *ApJS*, 155, 351
- Sembach, K. R., Wakker, B. P., Savage, B. D., et al. 2003, *ApJS*, 146, 165
- Somerville, R. S., & Davé, R. 2015, *ARA&A*, 53, 51
- Stevens, I. R., & Hartwell, J. M. 2003, *MNRAS*, 339, 280
- Stocke, J. T., Keeney, B. A., Danforth, C. W., et al. 2013, *ApJ*, 763, 148
- Strickland, D. K., & Heckman, T. M. 2009, *ApJ*, 697, 2030
- Sutherland, R. S., & Dopita, M. A. 1993, *ApJS*, 88, 253
- Thom, C., & Chen, H.-W. 2008, *ApJS*, 179, 37
- Thompson, T. A., Quataert, E., Zhang, D., & Weinberg, D. H. 2016, *MNRAS*, 455, 1830
- Thornton, K., Gaudlitz, M., Janka, H.-T., & Steinmetz, M. 1998, *ApJ*, 500, 95
- Tremonti, C. A., Heckman, T. M., Kauffmann, G., et al. 2004, *ApJ*, 613, 898
- Tripp, T. M., Savage, B. D., & Jenkins, E. B. 2000, *ApJ*, 534, L1
- Tripp, T. M., Sembach, K. R., Bowen, D. V., et al. 2008, *ApJS*, 177, 39
- Tumlinson, J., Shull, J. M., Giroux, M. L., & Stocke, J. T. 2005, *ApJ*, 620, 95
- Tumlinson, J., Thom, C., Werk, J. K., et al. 2011, *Science*, 334, 948
- . 2013, *ApJ*, 777, 59
- Tuttle, S. E., Schiminovich, D., Grange, R., et al. 2010, in Society of Photo-Optical Instrumentation Engineers (SPIE) Conference Series, Vol. 7732, Society of Photo-Optical Instrumentation Engineers (SPIE) Conference Series, 773227
- Wakker, B. P., & Savage, B. D. 2009, *ApJS*, 182, 378
- Weiner, B. J., Coil, A. L., Prochaska, J. X., et al. 2009, *ApJ*, 692, 187
- Wold, I. G. B., Barger, A. J., & Cowie, L. L. 2014, *ApJ*, 783, 119
- Yin, S. Y., Liang, Y. C., Hammer, F., et al. 2007, *A&A*, 462, 535
- Zahid, H. J., Dima, G. I., Kewley, L. J., Erb, D. K., & Davé, R. 2012, *ApJ*, 757, 54

APPENDIX
MATCHING THE POINT SPREAD FUNCTION

The diffuse halo of O VI emission could be mimicked if the F125LP Point Spread Function (PSF) is broader than that of F140LP. We used custom software to match images to a common PSF. Point sources (stars) that are bright in the far UV are rare, making empirical studies of the SBC PSFs challenging, and the models available from STScI severely underestimate the power in the extended wings of the PSF (at radii larger than 1 arcsec). We instead build empirical PSF models by examining multi-epoch calibration data of the globular cluster NGC 6681. These were obtained under many programs by the ACS instrument team at STScI, stretching back to 2002 when the instrument was first mounted. We have obtained all the calibration images taken in F125LP and F140LP from the MAST, drizzled and stacked them using the same methods as for our science data. The total exposure time in F125LP is 13,530 seconds, and 7,350 seconds in F140LP. The brightest star in NGC 6681 has a FUV AB magnitude of 18.0, giving a countrate of 22 counts per second in the brightest pixel in F125LP. This is just below the non-linear regime of the SBC detector, indicating that calibration data are as good as possible for deriving the PSF. We then selected 45 (48) stars in the F125LP (F140LP) images, extracted stamps, and stacked them to produce a very deep point-source image. A model PSF consisting of a combination of three 2D functions (an elliptical Moffat function, a radially symmetric Gaussian function, and a symmetric fourth order polynomial function) was fitted to the stacked image using least squares fitting with the LMFIT package for Python1. The stacking was then redone iteratively with the contribution from nearby stars removed by subtracting the model PSF. The final stacked images in the two filters were normalized to have a total sum of 1 and are presented in Figure 12, while the final best fitting models were used to compute the matching convolution kernel.

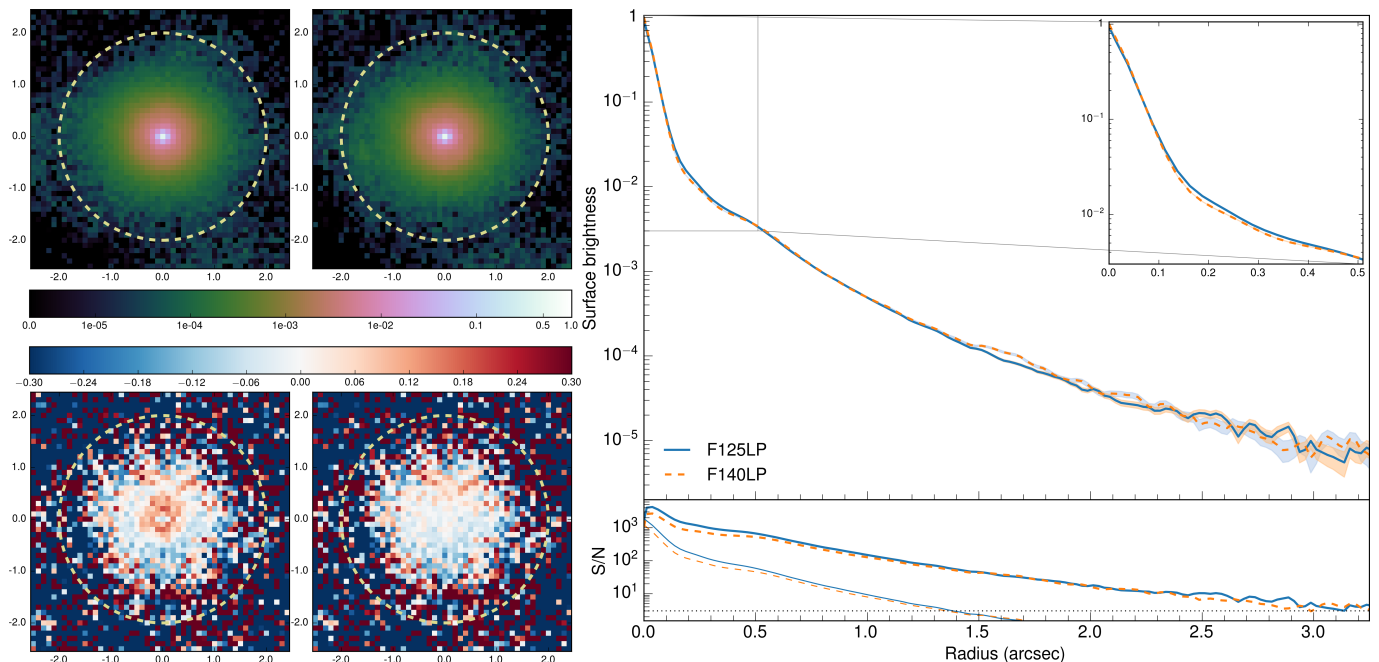


Figure 12. The Point Spread Function of the SBC Filters. The top left panels show the empirical PSF of the F125LP (left hand side) and F140LP (right hand side) filters in log scale. The bottom left panels show the relative difference map, $(F125LP - F140LP) / F140LP$, without any PSF matching on the left and with PSF matching on the right. Note that the 2D PSF models are only trustworthy (at a 3σ level) out to a radius of about 1.3 arcseconds. The top right panel shows the surface brightness profiles of the two empirical PSFs with the shaded regions showing the 1σ errors per annulus, and the inset showing the inner 0.5 arcseconds of the profile. The lower right panel shows the signal-to-noise (S/N) of the surface brightness profile (thick lines), and the average signal-to-noise measured in the 2D empirical PSFs within the same annuli used to compute the surface brightness profile (thin lines).

The right panel of Figure 12 shows the extracted radial surface brightness profiles of the empirical PSFs in F125LP and F140LP, demonstrating that there is a small difference between the filters in the inner 0.5 arcseconds of the PSF (shown in the inset), where the F125LP PSF is slightly more extended than the F140LP PSF, but no difference within the uncertainties in the outer parts of the profiles. The uncertainties for the radial profiles were estimated by adding the sky noise, measured in the stacked images, to Poisson noise, estimated from the PSF model, in quadrature. The azimuthally averaged profiles have a S/N of at least 3 out to a radius of 3 arcseconds. Note that in Figure 8 the net O VI emission begins significantly inside of this radius.

We then compute the relative difference between the filters as:

$$\mathcal{R}(r) = \frac{\Sigma(f_{F125LP,i} - f_{F140LP,i})}{\max(f_{F140LP})} \Big/ N \quad (\text{A1})$$

where f_{F125LP} and f_{F140LP} designate the flux in the two filters and summation is done over all pixels (N) inside a given radius r . \mathcal{R} is thus simply the difference in power per pixel at the given radii divided by the peak count rate. Within a radius of 0.5 arcseconds we find a \mathcal{R} value of 2×10^{-4} and within 3 arcseconds \mathcal{R} is 3×10^{-6} . This clearly shows that the difference between the PSFs mainly comes from the inner 0.5 arcseconds and not in the wings.

To account for the differences between the PSFs we compute convolution kernels that matches all of the filters to a common PSF (see 4.1.2). The lower part of the left panel in Figure 12 shows the relative difference map for the non-matched and matched cases. While the regions outside a radius of ~ 1.3 arcseconds (which is also seen in the S/N plot in the right panel) are too noisy for any meaningful comparisons to be made, the matching shows a substantial improvement for the inner part of the PSF. The \mathcal{R} ($r = 1$ arcsec) value for the matched case is 1×10^{-4} , roughly a factor of two smaller than in the non-matched case. At larger radius the changes to \mathcal{R} when matching is smaller because there is less difference to correct.

The surface brightness profiles in the right panel of Figure 12 shows that the PSF difference at a radius of ~ 2 arcseconds is extremely small and in fact negative (there is more flux in the F140LP than the F125LP PSF at that radius), with an \mathcal{R} value of -3×10^{-6} measured within an annulus around $r = 2$ arcseconds. However, there are some ‘‘bumps’’ in the F140LP radial profile (also visible in the 2D image of the PSF as the asymmetric emission at a radius ~ 1.5 arcseconds extending to the lower left) around this radius that are unlikely to be part of the true profile. These bumps are artifacts from stacking and gives rise to an additional systematic error (which will only add flux to the PSF) in the profile, which leads us to conclude that the difference at this radius is consistent with zero. Nevertheless, in our final O VI continuum subtraction we use PSF matched images that removes also this difference. It should be noted that even without the PSF matching, the difference at this radius is nowhere near enough to create the observed extended emission we detect.